SCIEPublish

*Article*

# Lithium-Rich Spinel Cathode with Higher Energy Density for Sustainable Li-Ion Batteries Operating in Extended Potential Range

**Somia M. Abbas [1], Motaz G. Fayed [2], Rasha S. El-Tawil [1], Saad G. Mohamed [2], Ashraf E. Abdel-Ghany [1], Ahmed M. Hashem [1], Alain Mauger [3] and Christian M. Julien [3,*]**

[1] Inorganic Chemistry Department, National Research Centre, 33 El Bohouth St., (Former El Tahrir St.), Dokki, Giza 12622, Egypt; somiamohamed119@yahoo.com (S.M.A.); r2samir@yahoo.com (R.S.E.-T.); achraf_28@yahoo.com (A.E.A.-G.); ahmedh242@yahoo.com (A.M.H.)

[2] Mining and Metallurgical Engineering Department, Tabbin Institute for Metallurgical Studies (TIMS), Tabbin, Helwan 109, Cairo 11421, Egypt; mezogmf@gmail.com (M.G.F.); saadmohamed@tims.gov.eg (S.G.M.)

[3] Institut de Minéralogie, de Physique des Matériaux et Cosmologie (IMPMC), Sorbonne Université, UMR-CNRS 7590, 4 Place Jussieu, 75752 Paris, France; alain.mauger@sorbonne-universite.fr (A.M.)

* Corresponding author. E-mail: christianjulien716@gmail.com (C.M.J.)

Received: 28 June 2024; Revised: 30 July 2024; Accepted: 28 August 2024; Available online: 2 September 2024

**ABSTRACT:** Lithium batteries pave way for rapidly reducing greenhouse gas emissions. Still there are concerns associated with battery sustainability, such as the supply of key battery materials like cobalt, nickel and carbon emissions related to their manufacture. While $LiMn_2O_4$ spinel is a common cathode material for Li-ion batteries that remove Co and Ni, studies on over-stoichiometric variants and their behavior across a broad potential range may be limited. Research in this area could provide valuable insights into the performance, stability and electrochemical characteristics of such cathodes, offering potential benefits for the development and optimization of Li-ion battery technologies. This study investigates the electrochemical behavior of Li-rich $Li_{1+y}Mn_{2-y}O_{4-\delta}$ (LMO, $y \approx 0.03$, $\delta \approx 0.01$) spinel as a cathode in Li-ion batteries, focusing on the phenomenon of extra capacity under the extended operating voltage 1.5–4.8 V vs. $Li^+/Li$. The nanostructured LMO sample synthesized by sol-gel method and calcined at 900 °C is characterized by X-ray diffraction, scanning and transmission electron microscopy and surface area measurements. The Li-rich spinel electrode delivers a specific discharge capacity of 172 mAh $g^{-1}$ at 1st cycle. It retains 123 mAh $g^{-1}$ at the 100th cycle (71.5% capacity retention) at current density of 100 mA $g^{-1}$ current density (i.e., ~0.7 C rate). An excellent stability is obtained in the 1.5–4.8 V potential window, with a discharge capacity of 77 mAh $g^{-1}$ after 500 cycles at the same current density, owing to the reduction of the Jahn-Teller effect by Li doping. These results contrast with the specific capacity of 85 mAh $g^{-1}$ (1st cycle) and the capacity retention of 54.3% after 100 cycles, obtained when the cell operates in the narrow potential range of 3.0–4.5 V.

**Keywords**: Li-rich $LiMn_2O_4$; Spinel; Cathode material; Lithium-ion battery



## 1. Introduction

Over the last four decades, lithium-ion batteries (LIBs) have emerged as the most successful power sources for various portable devices [1] and electric vehicles (EVs) [2]. Automotive LIB demand continues to riseg by about 65% to 550 GWh in 2022. By 2030, electricity demand for EVs will account for ~3.8% of global final electricity consumption [3]. One of the ongoing challenges in the field of EVs is the need to enhance the energy density, providing longer driving ranges, and improve the safety of lithium-ion batteries (LIBs). Optimizing the positive electrode material, specifically the cathode, is key to achieving these objectives. [4]. In particular, the pioneering work on $LiMn_2O_4$ was conducted by John B. Goodenough, K.M. Abraham, and coworkers, including M. M. Thackeray, in 1984. Their research laid the foundation for the understanding and developing spinel $LiMn_2O_4$ as a cathode material for LIBs [5]. $LiMn_2O_4$ has a moderate theoretical specific capacity of 148 mAh $g^{-1}$, high working voltage (~4 V vs. $Li^+/Li$), low cost, low toxicity, and high thermal stability/high safety [6,7]. $LiMn_2O_4$ was synthesized by facile synthesis methods such as sol-

https://doi.org/10.70322/ism.2024.10014

gel and solid-state, which improved its properties in terms of loading capacity and high rate capability during cycling due to the high purity and optimized morphology of the synthesized particles [8]. However, $LiMn_2O_4$ still faces challenges, particularly in terms of cycle stability and discharge-specific capacity, especially at high temperatures. These limitations can hinder its large-scale application, particularly in demanding conditions. Improving the overall performance and durability of $LiMn_2O_4$ cathodes is crucial for expanding their applicability in diverse energy storage applications.

Spinel $LiMn_2O_4$ has a three-dimensional (3D) cubic structure with $Fd\bar{3}m$ space group (s.g.), facilitating easy lithium-ion diffusion [9]. The practical, specific capacities observed for $LiMn_2O_4$ in the 4-V operating potential range typically fall between 80–120 mAh $g^{-1}$. This is notably lower than its theoretical capacity of 148 mAh $g^{-1}$ [10]. The difference between the theoretical and practical capacities is often attributed to various factors, including side reactions and structural changes. The poor cycling stability, as mentioned, was attributed to a combination of structural transformation and Mn dissolution driven by the disproportionation reaction of $Mn^{3+}$ and Jahn-Teller (J-T) distortion. Above 3 V, further lithiation of the $LiMn_2O_4$ host lattice is achieved through Li insertion into octahedral vacancies [11] to form the over-lithiated $Li_2Mn_2O_4$ compound with an increasing discharge capacity. Over-lithiation typically involves reducing $Mn^{4+}$ to $Mn^{3+}$. The severe J-T distortion, in turn, results in irreversible phase transformations within the LMO structure, often transitioning from a cubic phase to a tetragonal phase. These structural changes are associated with capacity fading and reduced cycling stability of $LiMn_2O_4$, making over-lithiation impracticable for long-term battery performance [12]. Furthermore, if additional lithiation occurs, the lithium salt ($LiPF_6$) can react with the electrolyte and any water present to produce HF and other acidic byproducts. These acids can lead to surface erosion and dissolution on the cathode, which in turn accelerates the rate of deterioration [13]. Bulk doping and surface coating techniques were used to stabilize the crystal structure, limit the Mn dissolution, and suppress the J-T distortion [14]. These techniques are effective above 3 V and less effective beyond one lithium intercalation below 3 V, as it is hard to suppress the severe J-T distortion. As a result, most previous research has primarily concentrated on electrochemical studies within the 4 V range for spinel $LiMn_2O_4$ cathodes [11]. The Li//$LiMn_2O_4$ cell cycles much better at 4 V than at 3 V but with slow capacity fading at this voltage. Liu and coworkers [15] stated that the tetragonal $LiMn_2O_4$ phase is thermodynamically unstable above 3 V. Still, there was evidence of its presence after cycling of Li//$Li_xMn_2O_4$ cells at a high rate between 4.5 and 3.5 V. They attributed the presence of this phase to kinetic constraints at the electrode surface during fast intercalation. Yu et al. [16] investigated the electrochemically synthesized single-crystalline and polycrystalline $LiMn_2O_4$ in the voltage range of 2.0–4.8 V vs. $Li^+$/Li. The single-crystalline $LiMn_2O_4$ exhibited a higher Li-ion storage capacity than polycrystalline $LiMn_2O_4$, particularly due to a large contribution at the 3-volt potential plateau. This indicates that the material's structural characteristics significantly impact its electrochemical performance.The interest in understanding the behavior of $LiMn_2O_4$ at potentials below 3 V is driven by the desire to explore the electrochemical performance of the material in a region that could be relevant for practical applications. Investigating the material's behavior at lower potentials can provide insights into its capacity, cycling stability, and potential challenges encountered during real-world battery operation.

The most intensively investigated monovalent doping ion is $Li^+$. Li-rich stoichiometric spinels $Li_{1+\delta}Mn_{2-\delta}O_4$ ($0 \leq \delta \leq 0.33$) was proposed by Gummow et al. [17] and others [18–33]. $LiMn_2O_4$ is prone to lithium over-stoichiometry, i.e., lithium excess at the manganese sites and $Mn^{3+}/Mn^{4+}$ disorder. Goodenough et al. [18] showed that an increase in the average oxidation state of Mn in $Li_{1+x}Mn_{2-x}O_4$ resulted in the suppression of the J–T distortion. Xia and Yoshio [24] showed that nonstoichiometric spinel $Li_{1+x}Mn_2O_4$ provides a slightly lower capacity of about 110 to 120 mAh $g^{-1}$ and ideal cycling behavior with mitigated capacity fading. Liu et al. [32] showed that Li-rich $LiMn_2O_4$ with lithium/manganese disorder and surface reconstruction could effectively suppress the irreversible phase transition and manganese dissolution. Replacing $Mn^{3+}$ at a Mn 16*d* site with $Li^+$ creates a lithium antisite $Li_{Mn}^{2-}$. The synthesis of $LiMn_2O_4$ near-equilibrium conditions is expected to result in a lithium over-stoichiometric compound with the composition $Li_{1+\alpha}Mn_{2-\alpha}O_4$ or, more explicitly, $Li[Mn_{2-\alpha}Li_\alpha]O_4$ or $Li^+[Mn_{1-3\alpha}^{3+}Mn_{1+2\alpha}^{4+}Li_\alpha^+]O_4^{2-}$.

In this composition, each negatively charged lithium antisite ($Li_{Mn}^{2-}$) is balanced by two two-hole polarons, resulting in an average manganese oxidation state greater than +3.5. This means $Mn^{4+}$ is slightly more prevalent than $Mn^{3+}$ [33]. The theoretical capacity will, therefore, decrease from 148 to 148(1−3α) mAh $g^{-1}$.

The electrochemical properties of transition-metal (*M*) oxides are known to vary with the ratio of Li/*M* as over-lithiation significantly affects the float durability and cyclability of cathode materials; cells show slightly smaller capacity but superior cycle life and improved Coulombic efficiencies [34,35]. Kopec et al. [29] explored the relationship between chemical bonding, the average oxidation state of Mn cations, and lithium substitution in a series of lithium-rich manganate spinels. These spinels show a non-linear decrease in the crystallographic cubic parameter, which is due to the addition of extra $Li^+$ ions into 16*d* sites and the replacement of larger $Mn^{3+}$ ions with smaller $Mn^{4+}$ ions.The local

structure studied by FTIR shows an increase in the covalent bonds in $MnO_6$ octahedra of the spinel lattice. Dygas et al. [27] demonstrated that the strength of charge carrier relaxation in $Li_{1+x}Mn_{2-x}O_4$ is greater than in stoichiometric $LiMn_2O_4$.

Building upon the aforementioned affinity, the current study delves into the electrochemical performance of $Li_{1+y}Mn_{2-y}O_{4-\delta}$ ($y = 0.03$; $\delta = 0.01$) synthesized by ethylene-diaminetetraacetic acid (EDTA)-assisted sol-gel method to explore the effect of Li over-stoichiometry on the electrochemical behavior under extended potential range. The first stage of this research was to test the best sample which satisfies the structural criterion for high electrochemical performance via the study of the crystalline microstrain. Results demonstrated that calcination of LMO at 900 °C minimizes the strain. For the first time, we successfully induced the formation of the tetragonal phase $Li_2Mn_2O_4$ through long-term electrochemical cycling (500 cycles) of the Li-rich spinel $Li_{1.03}Mn_{1.97}O_{3.99}$ in the wide voltage range of 1.5–4.8 V, taking advantage of this continuous and elusive phenomenon known as Jahn–Teller distortion. The electrochemical investigation revealed the formation of the lithiated phase $Li_{1.03+x}Mn_{1.97}O_{3.99}$ ($x \approx 1$) when the potential dropped below 3 V, resulting in a capacity of 172 mAh $g^{-1}$ nearly double that observed at 3 V (85 mAh $g^{-1}$). The newly identified phase exhibited significantly improved capacity retention compared to the ideal spinel $LiMn_2O_4$ cycled above 3 V. The synthesized Li-rich $Li_{1+y}Mn_{2-y}O_{4-\delta}$ (LMO) spinel was characterized using X-ray diffraction (XRD), thermogravimetric analysis (TGA), scanning electron microscopy (SEM), high-resolution transmission electron microscopy (HRTEM), and surface area (BET), to elucidate their morphological and structural properties. Additional electrical and electrochemical characterizations of the as-prepared LMO sample are presented, including cyclic voltammetry (CV), galvanostatic charge-discharge (GCD), electrochemical impedance spectroscopy (EIS), and area-specific impedance (ASI).

## 2. Materials and Methods

### *2.1. Material Synthesis*

Lithium manganese oxide powders were prepared using the sol-gel method (SGM), as illustrated in Figure 1. The precusor was fabricated using lithium acetate (analytical Rasayan. S.d. FINE-CHEM Ltd., Mumbai, India), manganese acetate (Sigma Aldrich, Burlington, MA, USA) and ethylene diamine tetraacetic acid (EDTA) (Sisco Research Laboratories Pvt. Ltd., Mumbai, India) as chelating agent. Lithium acetate and manganese acetate were dissolved in 100 mL distilled water with stirring for 1 h. The molar ratio of Li/Mn was adjusted to 1.05:2. An excess of 5 mol% Li was employed to account for potential mechanical and volatilization losses during subsequent transportation and calcination. The molar ratio of the chelating agent to the total metal ions was set to unity. The solution's pH was then adjusted to 7 using an alkaline ammonium hydroxide solution. EDTA was dissolved and added drop by drop to the continuously stirred solution of dissolved metal ions. Subsequently, the prepared solution was evaporated at 80 °C with magnetic stirring until a transparent sol was obtained. With further water evaporation, the sol transforms into a viscous and transparent gel. The resulting gel precursor was first heated in air at 450 °C for 5 h to eliminate the organic materials, then ground and recalcined at 750 °C for 5 h. Final calcination was carried out in air at 900 °C for 10 h with intermittent grinding (noted LMO900). For comparison, two samples were also prepared at lower calcination temperatures of 400 and 700 °C.

### *2.2. Material Characterization*

The phase and structure of the samples were analyzed by X-ray diffraction (XRD) using a Philips X'Pert apparatus equipped with a $CuK_\alpha$ X-ray radiation source ($\lambda = 1.54056$ Å). Data were collected in the $2\theta$ range 10–80° at a step of 0.05°. The obtained XRD patterns were refined using the FULLPROF software (Toolbar Fullprof suit program (3.00), version June-2015) [36]. TGA measurements were carried out using a thermal gravimetric analyzer (Perkin Elmer, TGA 7 series) in the temperature range of 30–1000 °C in the air at a heating rate of 10 °C $min^{-1}$. The surface morphology of the fabricated samples was visualized using field emission scanning electron microscopy (Quanta, FEG 250). The microstructure and morphology of the materials were observed with a JEOL 2100F microscope operated at 200 kV and equipped with a Cs corrector to achieve atomic resolution better than 0.14 nm. Particle-size distribution was analyzed using the ImageJ software [37]. BET surface area and pore size distribution of synthesized samples were determined from $N_2$-adsorption experiments using (Belsorp max version 2.3.2). The BET surface area was calculated from the isotherms ranging from 0.02 to 0.4 of relative pressures ($P/P_0$). Using the Barrett-Joyner-Halenda (BJH) model, the pore volume and size distribution were derived from the adsorption branches of the isotherms, and the total pore volumes were estimated from the adsorbed amount at a relative pressure $P/P_0$ of 0.995.

The cathode material was prepared for electrochemical testing by casting a slurry composed of 80 wt.% LMO active material, 10 wt.% carbon black (Super P) or C65 (TIMCAL), and 10 wt.% polyvinylidene fluoride (PVdF) mixed with a few drops of N-methyl-2-pyrrolidone (NMP). The Al foil used as a current collector was put on a flat glass. The mixture slurry was pasted onto the Al foil and then dried in a vacuum oven. Sheets of Ø 12 mm circular pieces of positive electrode materials were used as working electrodes with areal mass loading in the 1.2–1.3 mg $cm^{-2}$ range. The electrochemical properties of LMO electrodes were carried out using 2032-type coin cells. Non-aqueous Li//LMO cells were assembled in an argon-filled glove box, with Li foil as a combined counter and reference electrode and Whatman GF/D borosilicate glass fiber as the separator. The aprotic electrolyte consisted of 1 mol $L^{-1}$ $LiPF_6$ dissolved in ethylene carbonate and dimethyl carbonate (EC: DMC; 1:1 *w*/*w*). 0.67 C (100 mA $g^{-1}$) was used as C-rate for cycling testing, and 0.2 mV $s^{-1}$ as the scan rate for cyclic voltammetry testing. The cells were subjected to galvanostatic charging and discharging using a NEWARE BTS-4000 battery testing equipment between 4.8 and 1.5 V at 20 °C under various current densities (0.148 A $g^{-1}$ is equivalent to 1C rate). The potentials reported in this work refer to the $Li^+$/Li redox couple.

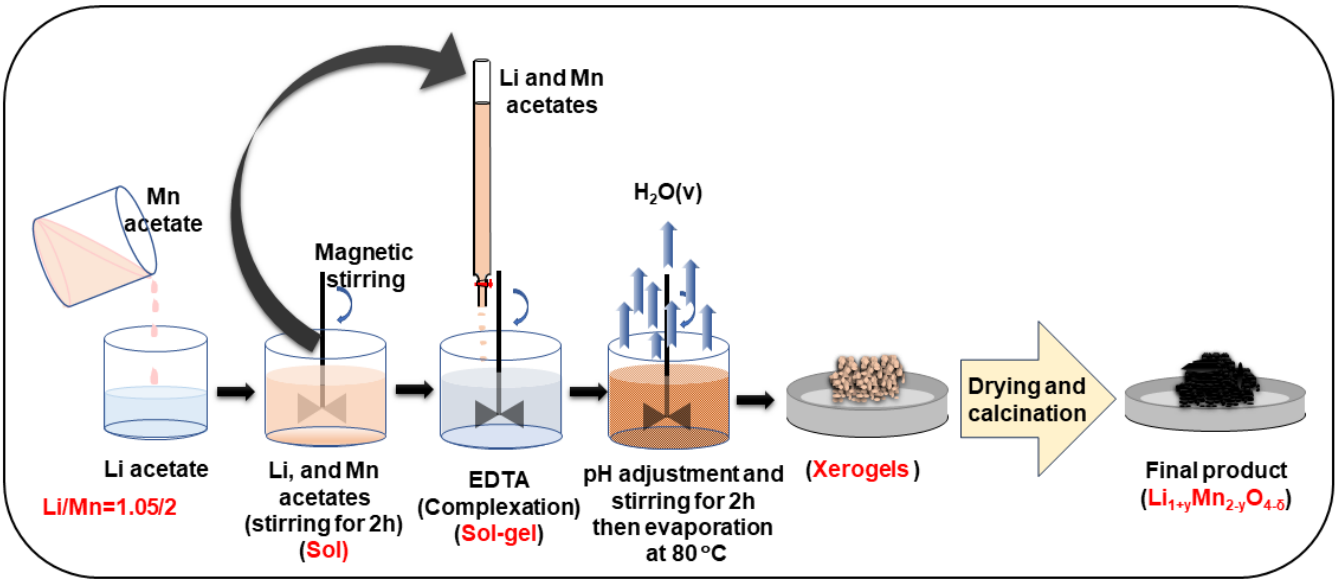


**Figure 1.** Illustration of the synthesis procedure for Li-rich LMO.

## 3. Results

### *3.1. Structural and Compositional Properties*

XRD pattern for the LMO900 sample synthesized by sol-gel method using EDTA as a chelating agent at annealing temperature of 900 °C is shown in Figure 2a. In the 2θ range 10–80°, the XRD patterns reveal eight intense peaks located at 18.7°, 36.1°, 37.7°, 43.7°, 48.1°, 58.1°, 63.8°, and 67.1°, which correspond to the (111), (311), (222), (400), (422), (511), (440), and (531) crystal planes of the $LiMn_2O_4$ spinel phase, respectively. The XRD reflections of the LMO material calcined at 900 °C are indexed according to the single spinel $LiMn_2O_4$ phase with cubic structure $Fd\bar{3}m$ ($O_h^7$) (JCPDS card No. 35-0782). The diffraction peaks corresponding to the (111), (311), and (400) lattice planes serve as the primary features of the spinel $LiMn_2O_4$ phase. In this phase, Li ions occupy the tetrahedral 8*a* sites (Wyckoff notation), Mn ions are distributed at octahedral 16*d* sites, and oxygen anions are located at the 32*e* sites [7]. Notably, the pure spinel phase is achieved during the transformation of the solid $Mn_3O_4$ → $LiMn_2O_4$ after calcination at 900 °C. The cubic lattice parameter *a* was calculated via the least square method using 10 well-defined reflections with indexation in the cubic structure. The crystallographic results summarized in Table 1 match well with the literature data [38–43]. The intensity ratio of $R_{int} = I_{(311)}/I_{(400)}$ is thought to be closely related to the electrochemical performance of spinel $LiMn_2O_4$. LMO900, with $R_{int} = 0.87$, is expected to exhibit good electrochemical performances.

In contrast, samples heat treated at 450 and 750 °C display additional reflections at $2\theta \approx 32°$ attributed to $Mn_3O_4$ impurities in their XRD patterns. The peaks associated with the $LiMn_2O_4$ spinel phase are well-defined but slightly broadened, indicating the formation of nanosized grains with significant lattice strain. These features do not satisfy the structural criterion of an optimized electrode and are unfavorable for high electrochemical performance to attain high-rate capability and cycling stability [38]. Raising the annealing temperature to 900 °C results in a gradual sharpening

of all peaks, signifying an enhancement in crystallinity with local structure ordering, grain size growth, and/or release of lattice strain. The lattice parameter slightly increases from 8.2322 to 8.2449 Å during calcination from 700 to 900 °C.

**Table 1**. XRD data for the spinel sample synthesized by EDTA-assisted sol-gel method at 900 °C in air.

| Structural Properties | LMO900 |
|---|---|
| Lattice parameter *a* (Å) | 8.2449(2) |
| Unit cell volume (Å$^3$) | 560.47 |
| Crystallite size (nm) | 65 ± 1 |
| Strain × $10^{-3}$ (rd) | 0.72 |
| FWHM (400) | 0.182 |
| $I_{(311)}/I_{(400)}$ | 0.87 |

Additionally, the structure and composition of the LMO900 sample have been examined through Rietveld refinement (Figure 2a). The small values of the residual and reliability factors ($R_p$ = 8.36%, $R_{wp}$ = 11.87%, and $\chi^2$ = 1.41) in the Rietveld analysis indicate the successful identification of the cubic phase. The difference between the calculated and experimental diffractogram (blue curve) demonstrates the quality of the fit, validating the structural model. Results indicate an under-occupancy of Mn and a smaller unit-cell parameter ($a$ = 8.2449 Å) compared to that for a perfect spinel structure for stoichiometric $LiMn_2O_4$ ($a_0$ = 8.24762 Å and $V_0$ = 561.03 Å$^3$). This suggests that the LMO900 sample is Li doped and has the composition $Li_{1.03}Mn_{1.97}O_{3.99}$ with 3 mol.% excess of Li. This composition implies the substitution of excess Li ions onto the Mn 16*d* site in the spinel, resulting in an average Mn oxidation state of 3.54 [17].

Additional structural parameters are worth considering to quantify the residual lattice strain and describe the slight variation (if it exists) caused by increased calcination temperature.

First, the full-width at half-maximum (FWHM) of the (400) peak at 2θ = 43.7° is highly sensitive to both the calcination temperature and the degree of crystallization and local structural order. Therefore, as reported by several reports, the lower value of the FWHM of the (400) peak is related to higher crystallinity and better ordering of the local structure [30,31]. It is noted that the FWHM of the (400) peak decreases with increasing calcination temperature, indicating that both crystallinity and local structure ordering of the LMO900 sample is the largest among all samples. cubic lattice parameters and crystallite size increase. The lattice parameter increase is attributed to a significant expansion of the spinel lattice, which matches well with previous $LiMn_2O_4$ reports [29,32], while the increase in the crystallite size may be due to a residual lattice strain.

Broadening of diffraction peaks is the third fingerprint of the crystallinity of $LiMn_2O_4$ powders and the homogeneous distribution of cations within the structure. The microstrain (ε) of the LMO900 particles was determined using the Williamson-Hall equation [44]:

$$B_{hkl} \cos \theta_{hkl} = (K\lambda/L_c) + 4\varepsilon \sin \theta_{hkl} \quad (1)$$

where $B_{hkl}$ is the line broadening of a Bragg reflection (*hkl*), $K$ = 0.9 is the shape factor for a spherical particle, $L_c$ is the crystallite size, and λ is the X-ray wavelength. The microstrain is estimated from the slope of the plot ($B_{hkl} \cos \theta_{hkl}$) vs. ($4\sin\theta_{hkl}$), and the intersection with the vertical axis provides the crystallite size (Figure 2b). The $B_{hkl}$ value used here is the instrumental corrected one. The microstrain (ε) is inversely proportional to the calcination temperature. The small value of the LMO900 microstrain ε = 0.72 × $10^{-3}$ rd depicts that the local field strain was decreased as a result of lattice ordering upon calcination at 900 °C. It can be compared to ε = 1.5 × $10^{-3}$ rd for $LiMn_2O_4$ synthesized via two-step precipitation method [45], to ε = 10.7 × $10^{-4}$ rd for $LiMn_2O_4$ prepared via rapid calcination of oxalates at 800 °C [46], and to ε = 1.3 × $10^{-3}$ rd for $LiMn_2O_4$ prepared through solid-state reaction of the $MnO+Li_2CO_3$ mixture [47]. This result is consistent with the crystallite size that was previously discussed. Comparing the lattice parameter *a*, FWHM of (400) peak, strain values, and $I_{(311)}/I_{(400)}$ ratio value of spinel lithium manganese oxides obtained by sol-gel method at different temperatures, we can conclude that the sample (LMO900) prepared at high temperature is well crystallized. This sample exhibits a crystallite size of 65 ± 1 nm determined by the Scherrer formula and shows a lower degree of particle agglomeration due to the synergetic effect of the post-annealing. LMO synthesized at 900 °C is expected to show better electrochemical performance than samples calcined at lower temperatures [48].

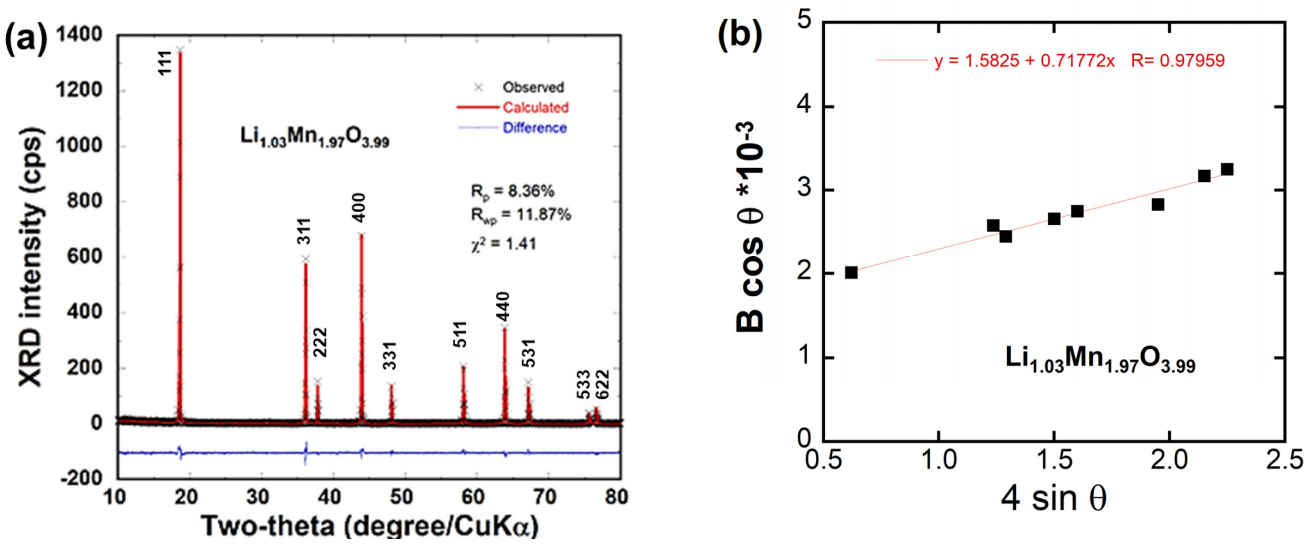


**Figure 2.** Structural properties of the LMO900 sample. (**a**) Rietveld refinement of the XRD pattern. The × signs show experimental data and the continuous line overlapping them refers to the calculated data. The difference between the experimental and calculated data is shown at the bottom. The reliability factors are $R_{wp}$ = 11.87%, $R_p$ = 8.36% and $\chi^2$ = 1.41. (**b**) Microstrain of the LMO particles calculated according to Equation (1).

### *3.2. Thermal Analysis*

In order to obtain complementary information on the exact temperature of the phase formation reaction of the spinel phase, we have performed a combined thermal gravimetry analysis (TGA) and differential thermal analysis (DTA) on the dried precursor complex in the temperature range 30–1000 °C. The results are shown in Figure 3a. The TGA curve shows two distinguishable transformation enthalpies, i.e., two weight loss steps occurring at ca. 100 and 235 °C. The endotherm observed at about 100 °C accompanied by a noticeable weight loss (3.1%), is attributed to the evaporation of residual water due to the hygroscopic nature of the precursor sample. As the heating process continues, an exothermic transformation begins to appear at around 235 °C, indicating the onset of the decomposition and/or the soft oxidation of the molecular precursor [49]. At 378 °C, a significant exothermic reaction occurs due to the decomposition of the organic moieties present in the precursor complex (attributed to the EDTA agent). This reaction occurs in the presence of atmospheric oxygen (in the air) and leads to a weight loss of over 50%s due to a violent oxidation-decomposition reaction. Eventually, this reaction results in the formation of the spinel structure. In this reaction, EDTA seems to function as a fuel in the pyrolysis of the molecular precursors, accelerating the decomposition process of all reactants. This behavior is characteristic of wet-chemistry synthesis using chelating agents such as glycolic, adipic, and oxalic acid [50,51]. The spinel phase begins to form at 370 °C due to the synergistic effect of all the reactants (lithium acetate and manganese acetate), as evidenced by the XRD analysis. The spinel remains stable from nearly 370 °C to 930 °C without any observable further weight loss.

The stability of the spinel structure is confirmed by the TG analysis of the as-prepared LMO900 sample (Figure 3b). No distinct weight loss in the TG curve is observed until 900 °C, indicating that the spinel phase formed by the sol-gel method using EDTA as a chelating agent has a stable structure. This stability has been reported in the literature [52]. Only slight weight loss of ~4% occurs above 900 °C, which may be attributed to the volatilization and liberation of lithium at such high temperatures. The concentration of the different elements deduced from the EDX spectrum shown in Figure 3c (O/M = 2.025) is consistent with results from Rietveld refinements.

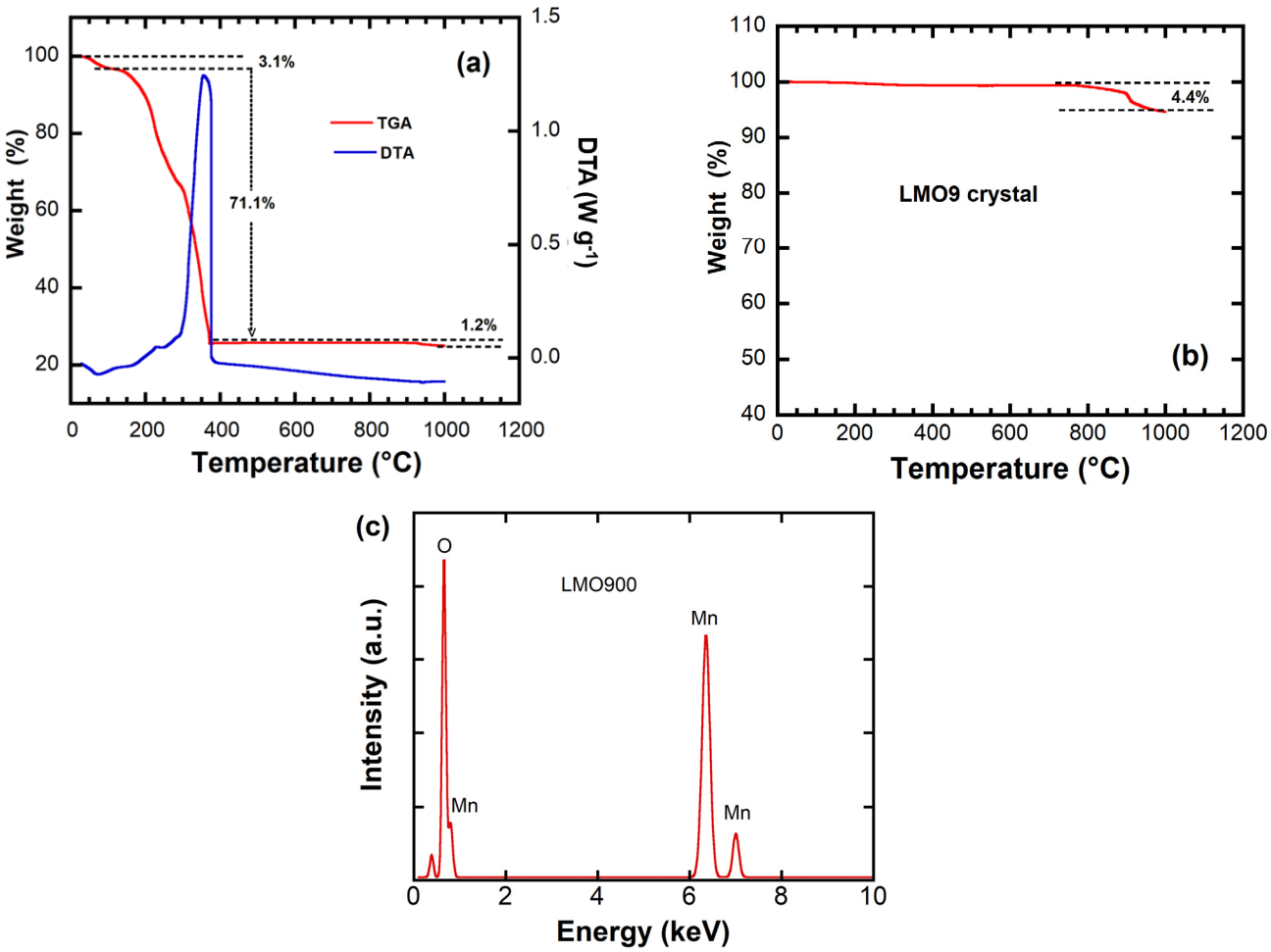


**Figure 3**. (**a**) TG/DTA curves of the dried precipitate Li-Mn-O precursor prepared by EDTA-assisted sol-gel method. Data are plotted in the "exotherm up" mode. (**b**) Thermal analysis of the LMO900 spinel sample. Experiments were conducted at a heating rate of 10 °C $min^{-1}$ in air. (**c**) EDX spectrum of the LMO900 sample.

### *3.3. Morphological Properties*

It is well known that particle size, surface morphology, and particle distribution are crucial factors influencing Li-ion battery performance. The electron microscopy analyses (SEM, TEM and HRTEM) of the LMO900 sample are presented in Figures 4 and 5, respectively. The SEM image (Figure 4a) reveals well-crystallized particles with similar morphology (almost monodisperse). LMO900 particles present a smooth surface with noticeable edges and corners. This material exhibits a truncated octahedral structure with a face-center cubic (fcc) framework. The particle size distribution was evaluated using the ImageJ software. SEM image analysis was conducted on approximately a hundred nanoparticles. The particles are uniformly dispersed with average size of ~380 nm, as shown in Figure 4b. These results indicate that the calcination process at 900 °C is beneficial for the growth of single-phase LMO crystals. Additionally, calcining at 900 °C combined with using EDTA as a chelating agent encourages the selective growth of the (110) and (100) crystal planes in LMO materials. This expands the diffusion channels for lithium ions, enhancing the material's electrochemical performance.The particles appear relatively large compared to spinel $LiMn_2O_4$ particles prepared by other synthesis methods [45,49], likely due to aggregation and agglomeration effects caused by the use of EDTA as a fuel, as illustrated before. The use of EDTA increases the surface energy during the calcination process, causing the crystalline grains to be adjacent and susceptible to anomalous growth. Features of truncated octahedral $LiMn_2O_4$ with face-center cubic structure, mainly exposing (111) planes and truncated with (100) and (110) planes, have been previously reported by several researchers [53–56]. They argue that the (111) planes, with thedensest Mn arrangements, are prone to form stable SEI layers, thereby suppressing Mn dissolution in the electrolyte. The tap density was determined by manually filling a graduated cylinder with the sample, followed by tapping to the constant volume of the sample in the cylinder. The tapped density of 1.85 g $cm^{-3}$ was calculated from the ratio between the sample mass and its final volume.

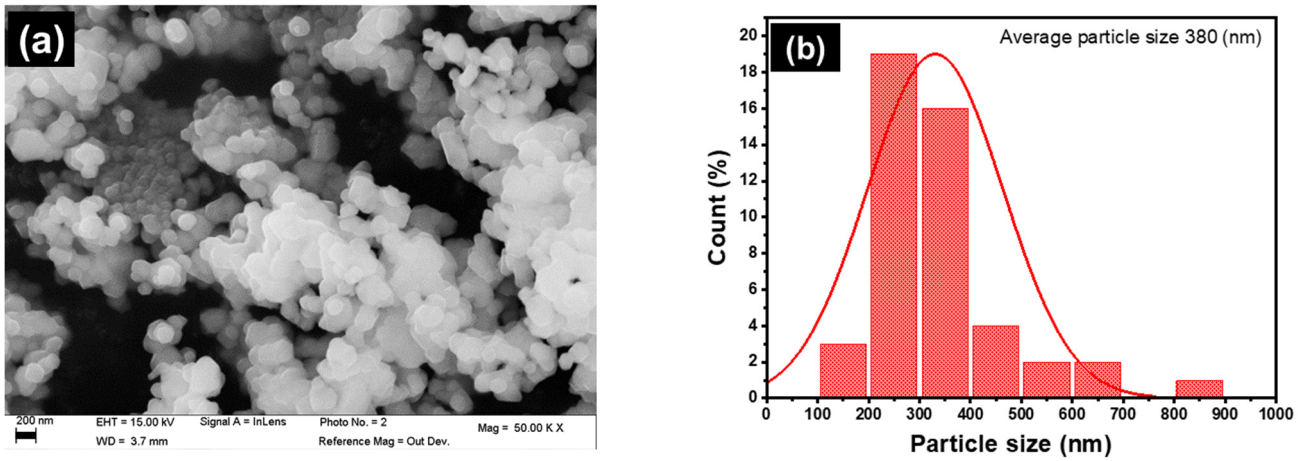


**Figure 4**. Morphology of the $Li_{1.03}Mn_{1.97}O_{3.99}$ sample. (**a**) FESEM image (scale of 200 nm). (**b**) Particle size distribution evaluated via ImageJ software.

To gain a deeper understanding of the structural information, the morphology and surface state of LMO particles were examined in detail by transmission electron microscopy (TEM). Figure 5a shows the TEM image of the LMO900 sample, further confirming the truncated octahedral structure with a uniform size distribution. The corresponding HRTEM images (Figure 5b,c) clearly exhibit lattice fringes with the *d* spacing of 0.457 nm, which matches well with the inter-planar distance of the (111) of LMO, indicating remarkable structural compatibility [46,47]. Therefore, LMO900 exhibits well-defined fringes, indicating the good crystallinity of powder. It has been reported that dominant (111) surfaces minimize Mn dissolution, facilitate $Li^+$ ions insertion/desertion, and reduce structural and volume change. Therefore, it can provide a superior cycle life and facilitate high discharge rate capabilities [57]. The related FFT pattern agrees well with the selected SAED pattern of the whole particle of LMO900 and shows well-defined spots, revealing its single crystalline nature (Figure 5d).

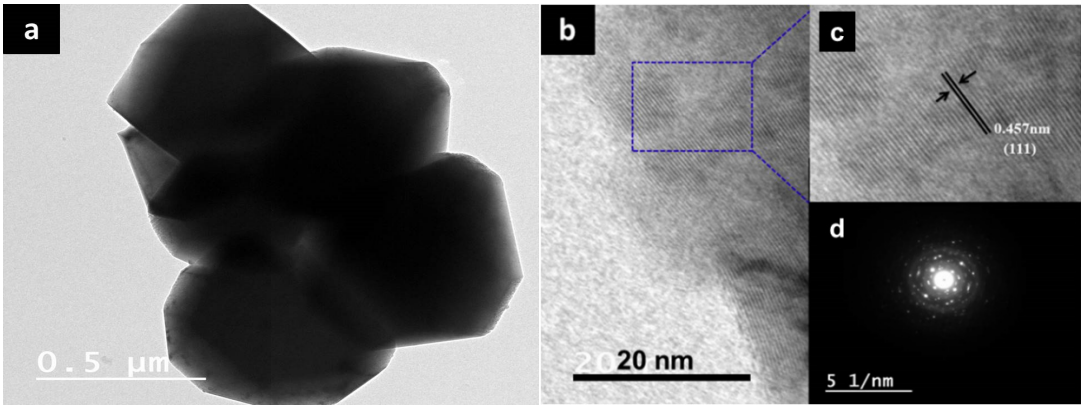


**Figure 5**. (**a**) TEM image of LMO900 particles, (**b**) HRTEM image showing the crystallographic structure, (**c**) enlarged HRTEM image showing the lattice fringes, and (**d**) SAED image.

The porosity of the synthesized LMO900 sample was investigated using the BET technique. Figure 6 presents the $N_2$ adsorption/desorption isotherm and the pore-size distribution (inset) for the LMO900 sample as a function of the relative pressure ($P/P_0$, $P_0$ is standard atmosphere pressure) measured at 77 K. The isotherm curves exhibit an increase in the amount of adsorbed $N_2$ with the rise in the $P/P_0$ value, accompanied by a hysteresis loop. This isotherm profile can be categorized as a type-IV curve with an H3-hysteresis loop, according to the IUPAC classification, implying the existence of a large number of mesopores. BET analysis shows that the LMO900 sample has a specific surface area of 1.68 $m^2\ g^{-1}$. This value is larger than previously obtained for $LiMn_2O_4$ synthesized at the same temperature via evaporation method-assisted oxalic acid as a precipitating agent [49]. Using the Barrett-Joyner-Halenda (BJH) model (via DFT method), the pore volume and size distribution were derived from the adsorption branches of the isotherms, and the total pore volumes were estimated from the adsorbed amount at a relative pressure $P/P_0$ of 0.995. As shown in the insets of Figure 6, the BJH pore size distribution reveals that the LMO900 sample possesses a mesoporous character, with monodisperse mesopore sizes estimated to be 5.1 nm with a total pore volume of $2.8 \times 10^{-3}$ $cm^3\ g^{-1}$. These features may be beneficial, allowing the electrolyte to fully penetrate the pores and facilitating efficient diffusion to active sites

with minimal resistance. Additionally, they can buffer the large volume changes during Li-ion insertion/extraction processes. Moreover, the uniformly interconnected mesopore size can decrease diffusion lengths by approximately 10 nm [58]. Note that particle size ($L_{BET}$ = 415 nm) can also be calculated from BET measurements by using the relationship $A = 3/(\rho L_{BET})$, where $A$ is the specific surface area, $\rho$ is the density (4.3 g cm$^{-3}$ for $LiMn_2O_4$).

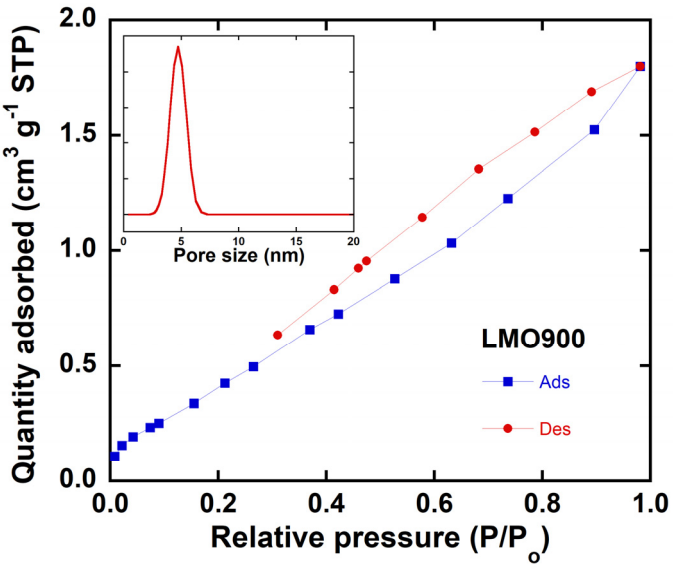


**Figure 6**. Nitrogen adsorption/desorption isotherms for LMO900. The inset displays the pore-size distribution.

### *3.4. Electronic State Analysis*

The electronic states of the elements in the spinel sample were revealed by X-ray photoelectron spectroscopy, as presented in Figure 7. The survey spectrum (Figure 7a) of the LMO900 specimen shows peaks with Gaussian-like line shape at binding energies of 84.5 eV for Mn 3s, 530.5 eV for O 1s, 55.0 eV for Li 1s, 642.3 eV for Mn $2p_{3/2}$, and 654.4 eV for Mn $2p_{1/2}$, which match well with the characteristic XPS patterns of the $LiMn_2O_4$ spinel phase [59]. The high-resolution XPS spectra of the Mn 2p, Mn 3s, and O 1s core levels for the spinel LMO900 sample are illustrated in Figure 7b–d, respectively. The experimental binding energies were corrected for specimen charging by referencing the C 1s line at 284.5 eV. As shown in Figure 7b, the Mn $2p_{3/2}$ and Mn $2p_{1/2}$ doublet of Mn 2p (with 11.6 eV spin-orbital energy separation) can be fitted in two bands corresponding to the binding position of $Mn^{3+}$ and $Mn^{4+}$ cations. The XPS spectrum of O 1s shown in Figure 7 corresponds to the (O-M-O) bonds. A shoulder peak observed at 530.9 eV is assigned to the residual oxygen related to impurities with $OH^-$ or $O^-$ bonding on the surface [60]. In order to accurately calculate the $Mn^{3+}$ and $Mn^{4+}$ contents, specific peaks of Mn $2p_{3/2}$ were fitted and the results are shown in Figure 7b and listed in Table 2. The average Mn valence state is 3.53 due to 53.2% $Mn^{4+}$ and 46.8% $Mn^{3+}$. Also, the exchange splitting value ($\Delta E_{3s}$) of Mn 3s can be used to determine the average valence state of Mn via a more quantitative method. According to Beyreuther et al. [61], there is a linear relationship between the Mn exchange splitting energy and Mn valence governed by the equation ($\nu_{Mn}$ = 9.67−1.27 $\Delta E_{3s}$/eV), which is used to approximately estimate the average valence state of Mn. Figure 7c shows that the $\Delta E_{3s}$ for LMO900 sample is ≈4.83 eV, corresponding to an average Mn valence state of 3.54. This result means that the excess 3 mol.% of Li is able to reduce the active J–T $Mn^{3+}$ ion, i.e., 3 mol.% of $Mn^{3+}$ is replaced by $Li^+$ on the Mn 16*d* site in the spinel framework. XPS results are consistent with the XRD data of the lithium-rich $Li_{1.03}Mn_{1.97}O_{3.99}$ phase.

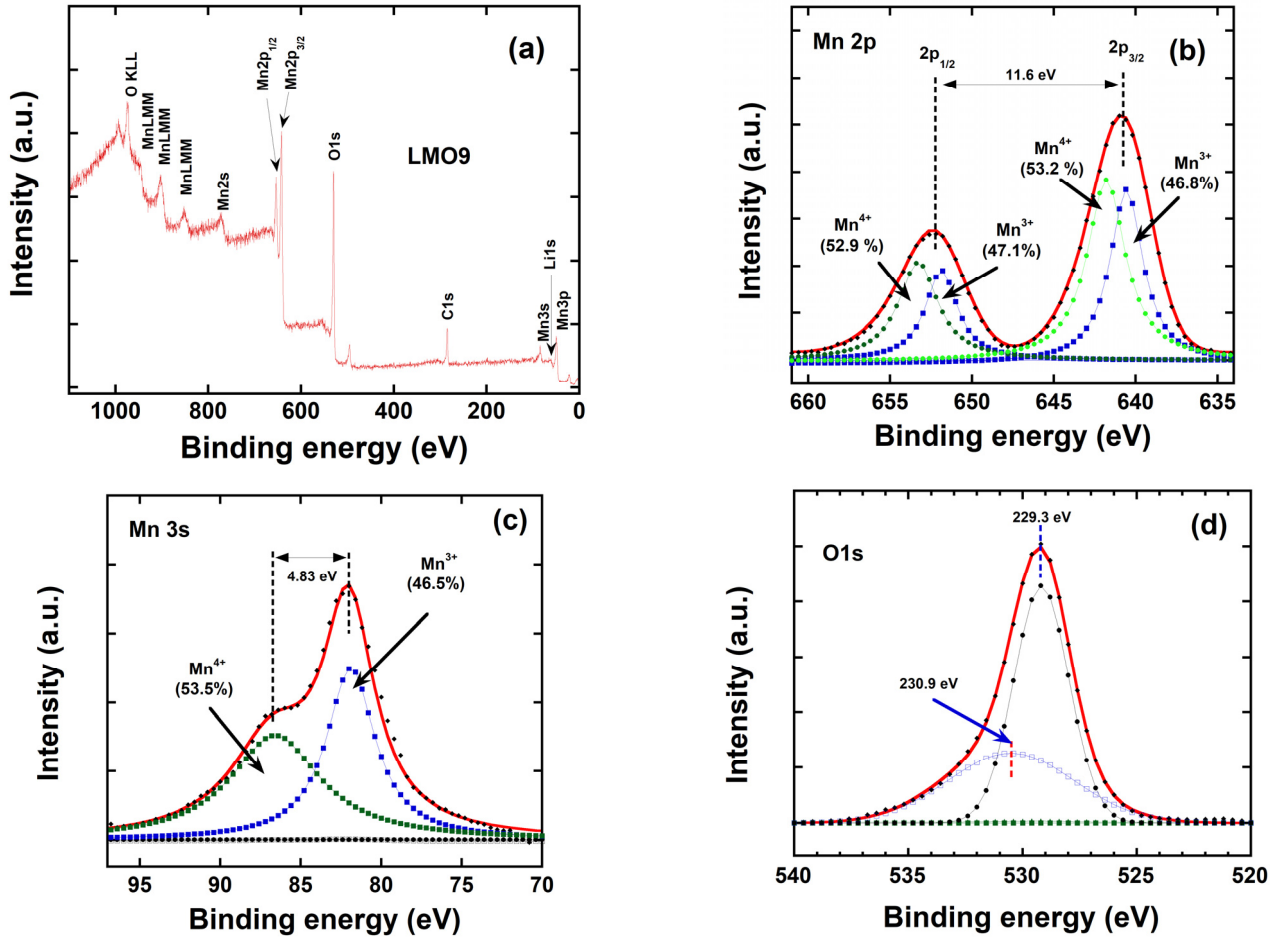


**Figure 7**. XPS results for the spinel LMO900 sample. (**a**) Survey spectrum and (**b**–**d**) high-resolution XPS spectra. (**b**) Mn 2p, (**c**) Mn 3s where deconvoluted bands represent the $Mn^{4+}$ (green) and $Mn^{3+}$ (blue) contribution, and (**d**) O1s core level spctrum where bands due to (O–M–O) bonds (black) and residual impurities (violet) are deconvoluted.

**Table 2**. Results of the XPS analysis for the spinel LMO900 sample: binding energies (eV) of Mn2p, atomic % of Mn and average Mn valance state obtained from Mn 2p and Mn 3s levels.

| Binding Energy (eV) | | | | Atomic % of Mn Species | | Average Mn Valance State | |
|---|---|---|---|---|---|---|---|
| $2p_{3/2}$ | | $2p_{1/2}$ | | | | | |
| $Mn^{3+}$ | $Mn^{4+}$ | $Mn^{3+}$ | $Mn^{4+}$ | $Mn^{3+}$ | $Mn^{4+}$ | Mn 2p Level | Mn 3s Level |
| 640.6 | 642.1 | 651.8 | 653.6 | 46.8 | 53.2 | 3.532 | 3.536 |

### *3.5. Electrochemical Performance*

Unlike previously published reports on Li-Mn-O spinels in the 4-V region [45,49,62], this work investigates the electrochemical properties of spinel $Li_{1.03}Mn_{1.97}O_{3.99}$ in both a narrow (3.0–4.5 V) and an extended (1.5–4.8 V) potential window using cyclic voltammetry (CV) and galvanostatic charge-discharge (GCD) method. Figure 8a displays the CV curves of the LMO900 electrode in the conventional voltage range of 3.0–4.5 V vs. $Li^+/Li$ at a sweep rate of 0.1 mV $s^{-1}$ over 4 cycles. All voltammograms exhibit two well-defined, separated reversible redox peaks at ~ 4.07/3.87 V and ~ 4.21/3.99 V. These peaks are associated with the reversible ingress and egress of $Li^+$ ions into/from the tetrahedral sites (8*a*) of the spinel lattice. Bianchini et al. [40] explored the phase diagram of a series of Li-Mn-O spinels. Stoichiometric $LiMn_2O_4$ undergoes two biphasic reactions, represented by the α + β and β + ε transitions, with ε < 0.1 close to λ-$Mn_2O_4$, with the intermediate β-phase close to $Li_{0.5}Mn_2O_4$ [63]. The same behavior is observed for the Li-rich compound $Li_{1.03}Mn_{1.97}O_{3.99}$, where the total amount of extractable lithium decreases as $1 - 3x = 0.91$. Therefore the amount of lithium that remains in the structure at the end of the charge increases to 0.12 (i.e., reaching the fully oxidized $Mn^{IV}$ composition $Li_{0.12}Mn_{1.97}O_{3.99}$).

On the other hand, Figure 8b displays the CV curves of the LMO900 material within the wide potential range of 1.5−4.8 V vs. $Li^+/Li$, using the same scan rate of 0.1 mV $s^{-1}$ over 6 cycles. The peaks become well-defined and sharper than those cycled at the narrow voltage window (3.0−4.5 V), and the high current response at the wider voltage window

was observed. Additionally, it has higher oxidation and reduction current peaks and a larger area, demonstrating the optimal reversibility of Li-ion transportation (i.e., Coulombic efficiency) and superior specific capacity. Besides the two redox peaks characteristic of the cubic stoichiometric spinel $LiMn_2O_4$ ($Fd\bar{3}m$ s.g.), there is notably the presence of an additional redox peak below the 3-V region at ~3.3/2.6 V, which remains stable over cycling. This additional redox reaction is a feature of the Li-ion storage at octahedral sites (16*c*), involving the conversion of cubic ($LiMn_2O_4$) to tetragonal phase transition ($Li_2Mn_2O_4$) [23,64]. This transformation results from an overlithiation case, in which 50% of $Mn^{4+}$:$d^3$ ($t_{2g}^3$) in the cubic structure converts to high spin $Mn^{3+}$:$d^4$($t_{2g}^3e_g^1$). This transformation is also confirmed by the oxidation and reduction current peak ratios ($I_{pa}/I_{pc}$) [63]. An additional oxidation peak at 3.8 V is attributed in the literature to parasitic reactions [65,66].

The peak potential difference ($\Delta E_p$) between the oxidation and reduction peaks can provide insights into the impedance growth related to electron transfer and the polarization degree of the battery [67]. The $\Delta E_p$ values of LMO900 cycled in the wide potential window 1.5–4.8 V are in the range 0.27–0.29 V, slightly larger than those of LMO900 cycled at the conventional potential range (0.19 V). This suggests that this sample may have a larger electrochemical reaction polarization, possibly due to the tetragonal phase ($Li_2Mn_2O_4$) presence. However, the sample exhibits similar lower potential intervals ($\Delta E_p$) over the subsequent five cycles, suggesting good stable cycle performance. On the other hand, $\Delta E_p$ values in the conventional narrow voltage range of 3.0–4.5 V decrease with cycling, indicating the stability of the cubic phase and the improvement of reversibility due to fast $Li^+$ ion transport. Therefore, we can conclude from the cyclic voltammograms of LMO900 that extra Li-ion storage at the 16*c* octahedral vacancies in spinel $LiMn_2O_4$ was more easily activated in the wide potential window (1.5–4.8 V), leading to the production of the tetragonal phase $Li_2Mn_2O_4$. This effect on the cycle performance will be investigated in detail in the following.

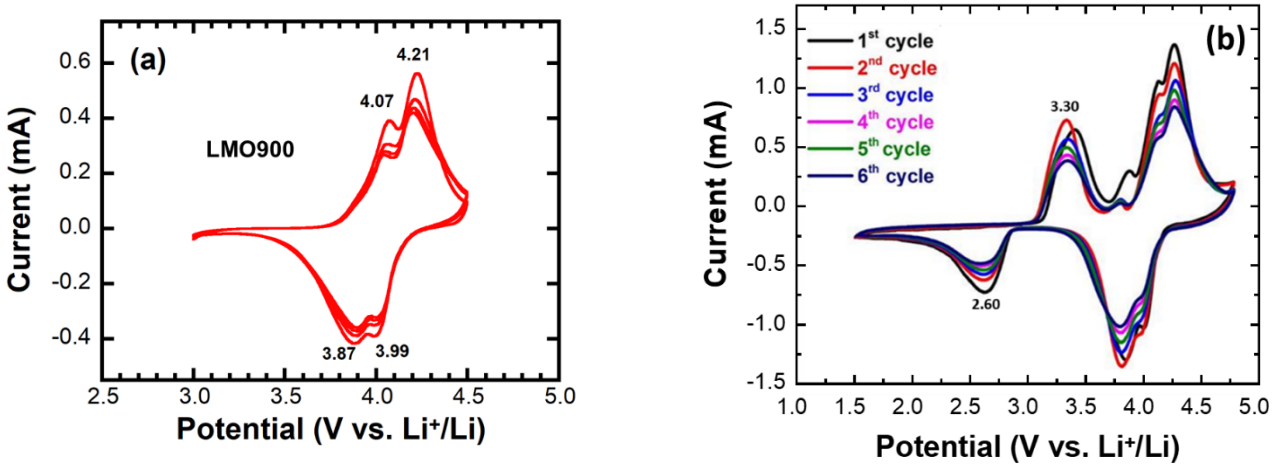


**Figure 8.** Cyclic voltammograms of the LMO900 electrode carried out at 0.1 mV $s^{-1}$ in the narrow 3.0–4.5 V (**a**) and extended 1.5–4.8 V (**b**) potential window.

The GCD profiles of the LMO900 electrode cycled at a current density of 100 mA $g^{-1}$ for 100 and 500 cycles in the potential range 3.0–4.5 V and 1.5–4.8 V vs. $Li^+$/Li are shown in Figure 9a,b, respectively. During the first charging and discharging process, Figure 9a displays two distinct voltage charge plateaus at ~4.10/4.20 V vs. $Li^+$/Li and two distinct voltage discharge plateaus at 4.05/3.94 V vs. $Li^+$/Li, respectively. These plateaus corresponding to the $LiMn_2O_4/Li_{0.5}Mn_2O_4$ and $Li_{0.5}Mn_2O_4/Li_\varepsilon Mn_2O_4$ two-phase systems match well with the CV results. For LMO900 operating in the wide voltage range of 1.5–4.8 V (Figure 9b), a slight polarization can be detected after 100 cycles. Notably, the polarization decreases over cycling. In the first 5 subsequent cycles, both charge and discharge voltage plateaus align with each other and with CV peaks. An additional plateau appears at ~2.8 V in the wide voltage range 1.5–4.8 V, corresponding to the tetragonal phase $Li_2Mn_2O_4$ and generally assigned as "3-V plateau" in literature [64]. The additional plateaus are consistent during the first five cycles and correspond to CV peaks. When cycled 100 times in the wide potential range of 1.5–4.8 V, the additional plateau gradually disappears, indicating gradual conversion of the tetragonal phase $Li_2Mn_2O_4$ to the cubic $LiMn_2O_4$. This result is also evident in the charge profile, as the plateau starts to disappear and takes on the shape of a charge profile of the 3.0–4.5 V range, accompanied by a decrease in polarization with repeated cycling.

Figure 9c,d illustrate the cycle stability and Coulombic efficiency of the LMO900 cathode material cycled at a current density of 100 mA $g^{-1}$ (approximately 0.7 C rate) within the narrow potential window 3.0–4.5 V and the

extended potential window 1.5–4.8V vs. $Li^+/Li$, respectively. Within the conventional voltage range of 3.0–4.5 V, the Li//LMO900 cell initially provides a specific capacity of 85 mAh $g^{-1}$, and after 100 cycles, it maintains 46 mAh $g^{-1}$. This corresponds to a capacity retention of 54.3%, with a significant capacity decay of 45.7% (equivalent to a capacity loss of approximately 0.46% per cycle). Remarkably, within the extended potential range of 1.5–4.8 V, the same cell exhibits an initial specific capacity of 173 mAh $g^{-1}$. After 100 cycles, it retains 123 mAh $g^{-1}$, resulting in a capacity retention of 71.45% and a minor capacity decay of 28.55%. The capacity loss is thus reduced to 0.28% per cycle. Note that such a cell provides a specific capacity of ~125 mAh $g^{-1}$ in the 3-V region. After 500 cycles, the Li//LMO900 cell gives 77 mAh $g^{-1}$ with a capacity retention of 44.6%. This test shows a small capacity decay of 0.15 mAh $g^{-1}$ per cycle. The findings suggest that a slight excess of Li in Mn 16*d* sites enhances specific capacity and reduces capacity loss by preventing J-T distortion in the Li-rich lattice.The observed increase in discharge capacity at lower voltage levels may be attributed to the presence of a tetragonal phase ($Li_2Mn_2O_4$), as the standard spinel ($LiMn_2O_4$) has a theoretical capacity of 148 mAh $g^{-1}$ for the insertion and extraction of 1 $Li^+$ per formula unit. In $Li_2Mn_2O_4$, an overlithiation state (2 $Li^+$ per formula unit) occurs, as Li ions can also insert into octahedral 16c sites, which are face-shared with tetrahedral 8*a* sites. This expanded capacity contributes to the increased discharge capacity observed in the lower voltage range.

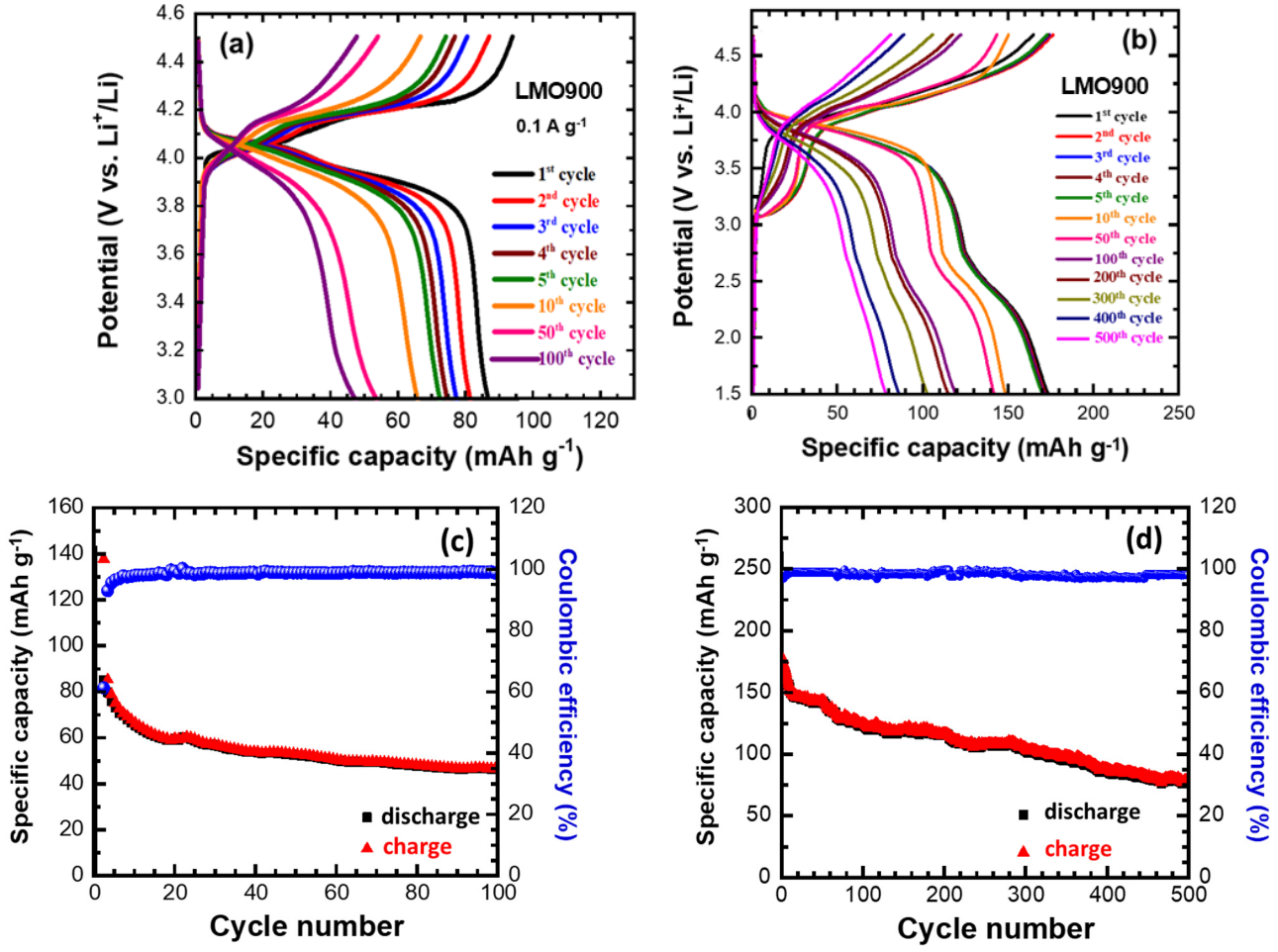


**Figure 9**. (**a**,**b**) GCD profiles of the LMO900 electrode recorded in the potential range of (**a**) 3.0–4.5 V for 100 cycles and (**b**) 1.5–4.8 V vs. $Li^+/Li$ for 500 cycles at current density of 100 mA $g^{-1}$ (0.7 C) (**c**,**d**) Cycleability and Coulombic efficiency of LMO900 cathode material in potential window (**a**) 3.0–4.5 V and (**b**) 1.5–4.8 V vs. $Li^+/Li$ under 100 mA $g^{-1}$ current density.

The representative GCD profiles of the LMO900 electrode tested in both potential domains at different current densities from 100 to 1000 mA $g^{-1}$ (with 1C = 148 mA $g^{-1}$) are depicted in Figure 10a,b. Even at high rates, the 4-volt plateaus remain recognizable. The GCD profiles of the spinel electrode cycled in the wide potential range show a remarkable phenomenon: the reduction of the plateau related to the tetragonal phase at 2.8 V (marked with an arrow in Figure 10b) until it disappears with increasing current density. This finding is attributed to the tetragonal phase behaving like a cubic phase under high current density conditions. Figure 10c shows the rate capability of the LMO900 electrode tested in the narrow potential range of 3.0–4.5 V. The discharge capacity values decrease with increasing C-rates in the sequence 85, 52, 35, 30, and 15 mAh $g^{-1}$ at 100, 200, 400, 500, and 1000 mA $g^{-1}$, respectively. When cycled again at

100 mA $g^{-1}$, the discharge capacity of the spinel sample reached 64.6 mAh $g^{-1}$ with a capacity retention of 76%. On the other side, LMO900 shows discharge capacity of 162, 135, 105, 83, and 58 mAh $g^{-1}$ (Figure 10d) when tested in the wide potential range 1.5–4.8 V using the same current densities at 100, 200, 400, 500 and 1000 mA $g^{-1}$, respectively. When cycled again at 100 mA $g^{-1}$, the discharge capacity of the spinel sample reached 148 mAh $g^{-1}$ with a capacity retention of 91.5%. Again, rate capability tests show much better performance for the wide-range voltage than the narrow one.

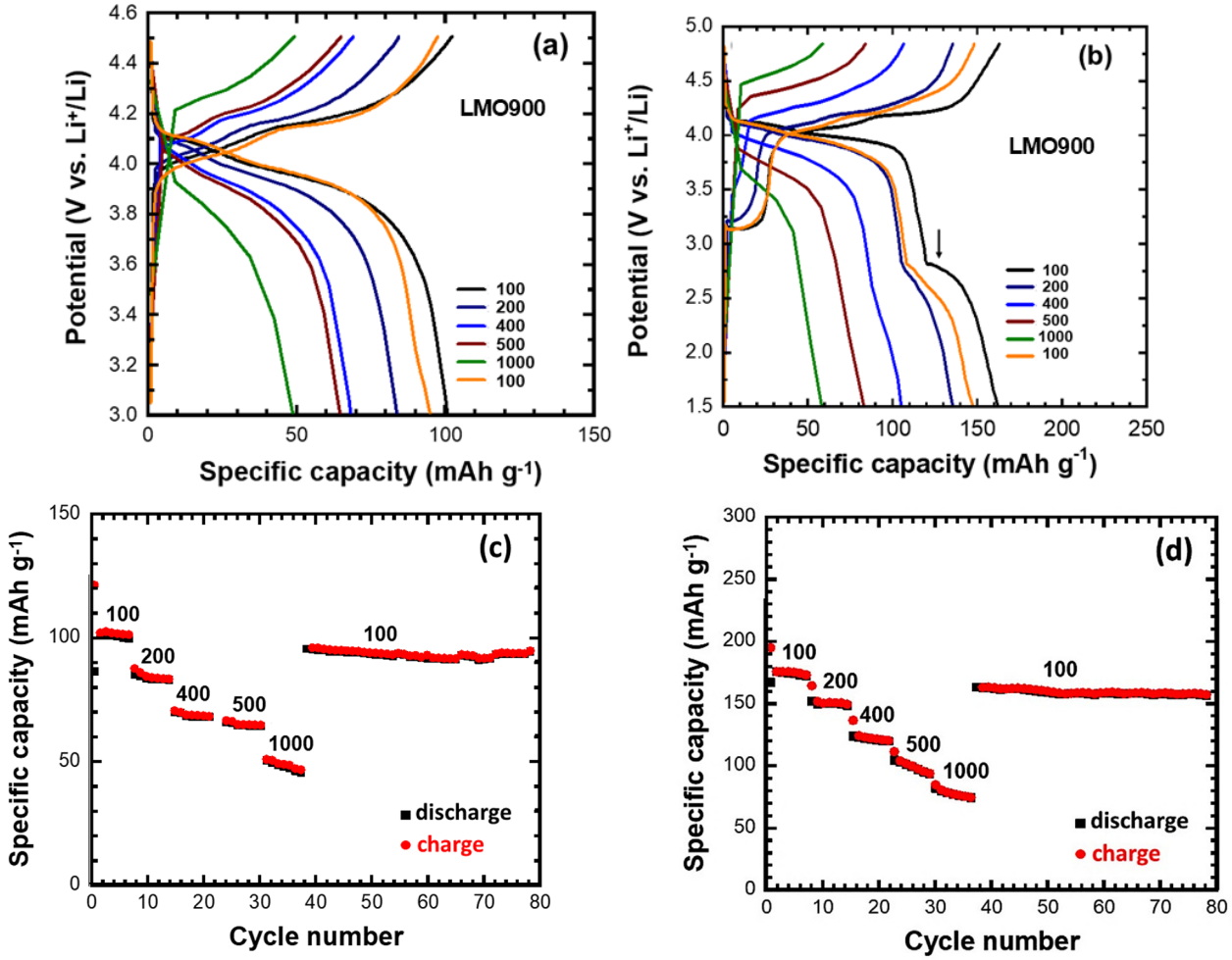


**Figure 10**. Electrochemical properties. (**a**,**b**) GCD profiles of the LMO900 electrode recorded in the potential range of (**a**) 3.0–4.5 V and (**b**) 1.5–4.8 V vs. $Li^+$/Li at different current densities (expressed in mA $g^{-1}$; 0.148 A $g^{-1}$ is equivalent to 1C rate). (**c**,**d**) Rate capability for different current densities (100–1000 mA $g^{-1}$) in potential window (**c**) 3.0–4.5 V and (**d**) 1.5–4.8 V vs. $Li^+$/Li.

### *3.6. EIS Measurements*

Electrochemical impedance spectroscopy is a useful *in-situ* technique to investigate the changes in the electrode-electrolyte interface resistance and $Li^+$ ion kinetics of electrodes (Figure 11). EIS measurements of LMO900 were carried out for the fresh electrode and after the 100th cycle for the voltage window 3.0–4.5. Additionally, measurements were performed after the 1st and 100th cycle for the voltage window 1.5–4.8 V, recorded at a rate of 0.7 C. Figure 11a,b show the Nyquist plots for 1.5–4.8 and 3.0–4.5 V, respectively. The equivalent circuit model used to analyze the EIS patterns (Figure 11e) is composed of four series components: the ohmic resistance of the cell ($R_s$), the impedance of the SEI layer ($R_{SEI}$-$CPE_{SEI}$ parallel circuit), the charge transfer impedance and interfacial capacitance at the electrode/electrolyte interface ($R_{ct}$-$CPE_{dl}$ parallel circuit), and the Warburg impedance ($Z_{w\text{-}R}$), which characterizes the $Li^+$ ion diffusion-controlled process [67]. In general, there is an increase in the total impedance after the 100th cycle at a 0.7 C rate, as shown from the fitted parameters listed in Table 3. For (1.5–4.8 V), the ohmic resistance ($R_s$) values are 2.85 and 4.17 Ω after the 1st and 100th cycle, respectively. Also, $R_{SEI}$ and $R_{ct}$ significantly increased during cycling. The real part $Z'(\omega)$ of the total impedance of the cell is the sum of the real part of the four components:

$$Z'(\omega) = R_s + R_{SEI} + R_{ct} + Z_w\,\omega^{-1/2} \quad (2)$$

$Z_w$ can be determined from the slope of the Warburg plot $Z'$ vs. $\omega^{-1/2}$ (Figure 11c,d), and the apparent diffusion coefficient $D_{Li}$ is given according to the relation [68]:

$$D_{Li} = \frac{R^2T^2}{2A^2n^4F^4C_{Li}^2Z_w^2} \quad (3)$$

in which $R$ is the gas constant, $T$ is the absolute temperature, $F$ is the Faraday constant, $n$ is the number of electrons transferred in the redox reaction at the electrode-electrolyte interface, $C_{Li}$ is the concentration of $Li^+$-ion inside the electrode, and $A$ is the effective surface area of the electrode. The apparent diffusion coefficient ($D_{Li}$) values for spinel electrodes, both in the initial (fresh) state and after the 1st and 100th cycles, are provided in Table 4. The data is presented for two voltage ranges, namely 3.0–4.5 V and 1.5–4.8 V. In the potential window of 3.0–4.5 V, the apparent diffusion coefficient for the fresh LMO900 electrode is $D_{Li} = 1.26 \times 10^{-12}$ cm$^2$ s$^{-1}$, which is higher than the value after the 100th cycle ($5.9 \times 10^{-13}$ cm$^2$ s$^{-1}$). This observation aligns with the increased values of $R_{SEI}$ and $R_{ct}$.

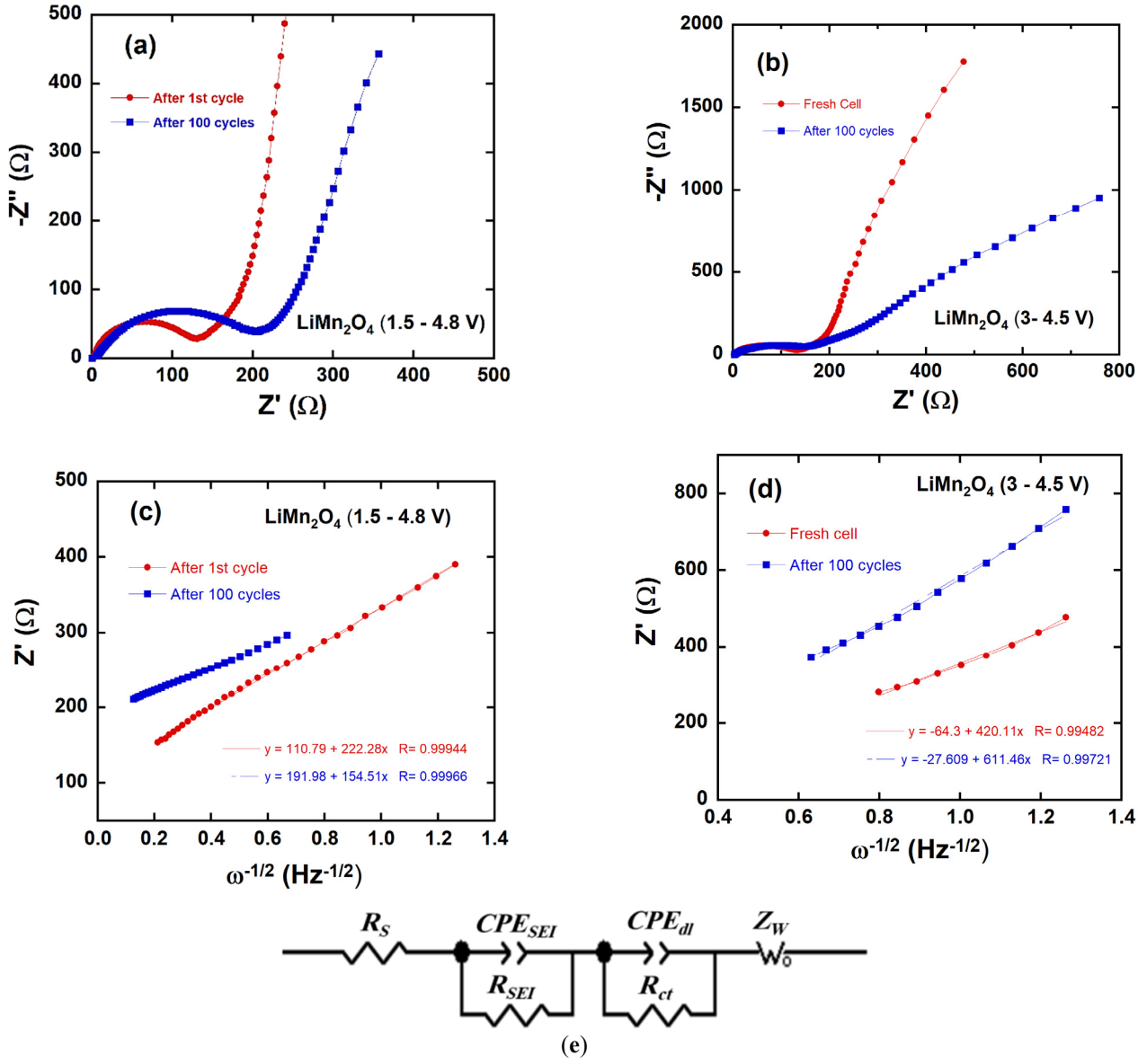


**Figure 11**. EIS measurements of LMO900 electrode (**a**) Nyquist plot after 1st and 100th cycle at 0.7 C rate, in the potential window 1.5–4.8 V. (**b**) Nyquist plot for fresh and after 100th cycle at 0.7 C rate, in the potential window 3.0–4.5 V. (**c**) Plots of the real part of the impedance vs. $\omega^{-1/2}$ for the LMO900 electrode after 1st and 100th cycle, in the potential window 1.5–4.8 V. (**d**) Plots of the real part of the impedance vs. $\omega^{-1/2}$ for LMO900 electrode for fresh and after 100th cycle, in the potential window 3.0–4.5 V. Full lines are the slope of the $Z_{real}$ vs. $\omega^{-1/2}$ fits, providing the Warburg impedance. (**e**) Equivalent circuit used for the analysis of the −Z" vs. Z' planes.

As reported previously, the value of $D_{Li}$ for fresh LMO spinel cathode material varies from $10^{-12}$ to $10^{-13}$ cm$^2$ s$^{-1}$ [45,61,69]. By raising the charge potential to 4.8 V and lowering the discharge potential to 1.5 V, the $D_{Li}$ of $4.53 \times 10^{-12}$

$cm^2\ s^{-1}$ after the 1st cycle of the LMO900 electrode is significantly lower than that after the 100th cycle ($6.2 \times 10^{-11}\ cm^2\ s^{-1}$). We recorded the Nyquist profiles after 1st cycle for the wide voltage window (1.5–4.8 V) because we anticipate a phase transition from cubic $LiMn_2O_4$ to a tetragonal or spinel-like structure (high Li concentration). This comparison confirms that the expansion of the voltage window (1.5–4.8 V) enhances $Li^+$ ion kinetics, possibly attributed to partial spinel-like ordering, $Li_{1+x}Mn_{2-x}O_4$, or a partial phase transition to $Li_2Mn_2O_4$ from the ideal spinel $LiMn_2O_4$. The deviation from the ideal spinel to a spinel-like or tetragonal structure increases the amount of $Li^+$ ions passing through tetrahedral sites or 16*c* octahedral sites without face-sharing Mn ions. This results in lower electrostatic repulsion compared to when $Li^+$ ions pass through tetrahedra that share faces with Mn ions, which leads to improved Li transport kinetics and, thus, a larger capacity.

**Table 3**. Fitting results of Nyquist plots of LMO900 cycled at 0.7 C rate in two potential widows.

| Parameters | LMO900 (1.5–4.8 V) | |
|---|---|---|
| | **After 1st Cycle** | **After 100th Cycle** |
| $R_s$ (Ω) | 73.1 | 89.5 |
| $R_{SEI}$ (Ω) | 53.2 | 66.1 |
| $CPE_{SEI\text{-}T}$ | $2.3 \times 10^{-6}$ | $1.4 \times 10^{-5}$ |
| $CPE_{SEI\text{-}P}$ | 0.960 | 0.743 |
| $R_{ct}$ (Ω) | 110.1 | 192.2 |
| $CPE_{dl\text{-}T}$ | $4.6 \times 10^{-4}$ | $4.0 \times 10^{-3}$ |
| $CPE_{dl\text{-}P}$ | 0.78 | 0.449 |
| $Z_{w\text{-}R}$ | 222 | 59.2 |
| $Z_{w\text{-}T}$ | 0.1653 | 0.033 |
| $Z_{w\text{-}P}$ | 0.458 | 0.393 |
| $D_{Li^+}$ ($cm^2\ s^{-1}$) | $4.5 \times 10^{-12}$ | $6.2 \times 10^{-11}$ |
| | **LMO900 (3.0–4.5 V)** | |
| $D_{Li^+}$ ($cm^2\ s^{-1}$) | $1.3 \times 10^{-12}$ | $5.9 \times 10^{-13}$ |

More information on the change in the overall cell potential as a function of the depth-of-discharge (DOD) can be obtained by evaluating the area-specific impedance (ASI) expressed in Ω $cm^2$, given by the following relation [70]:

$$ASI = A\frac{OCV - V_{cell}}{I} \quad (4)$$

where $A$ is the cross-sectional area of the electrode, $\Delta V = OCV - V_{cell}$ is the potential change during current interruption for 60 s at each DOD value, and $I$ is the current passed throughout the cell. Various factors can affect the area-specific impedance, including ohmic drop, Li-ion transport through the electrolyte, and solid-state diffusion within the electrode. Moreover, the ASI does not need to reach equilibrium conditions as in the case of EIS, which makes this technique more representative of the total internal resistance evaluation during cycling. Figure 12 displays the variation of ASI of the LMO900 electrode for the 1st and 100th cycles at 0.7 C rate in the narrow and extended voltage windows. At 20% DOD, the ASI values at the 1st cycle are 1.5 and 6 Ω and increased to 2.5 and 9.7 Ω, after the 100th cycle for the narrow and extended voltage window, respectively. At 90% DOD, the ASI value at the 1st cycle (5.7 Ω) increased to 17 Ω after the 100th cycle for the narrow voltage window (3.0–4.5 V). At the same DOD (90%), the ASI values at the 1st cycle (43.4 Ω) decreased to 39.4 Ω after the 100th cycle for the extended voltage window (1.5–4.8 V). These results indicate that the charge-transfer resistance is dependent on DOD as well as the aging of the electrode. This resistance increases systematically with increasing DOD, as noticed from the narrow voltage window 3.0–4.5 V. For the extended voltage range of 1.5–4.8 V, upon closer examination, as depicted in Figure 12, particularly in the 30–40% depth of discharge (DOD) range, a noteworthy shift (inversion) in the ASI behavior is observed at approximately 32% DOD. This entails a reduction in the ASI values with increased DOD, resulting in decreased charge-transfer resistance. This phenomenon facilitates smoother ion and electron transfer during the charge-discharge process. Comparing the discharge voltages, we observe a consistent increase in ASI values between the narrow and wide voltage windows until the discharge voltage reaches approximately 3 V, corresponding to 32% DOD. At this juncture, it is noteworthy that the voltage value for the wide voltage window is approximately 90% of the discharge voltage range observed in the narrow voltage window, as shown in Figure 12. Therefore, we conclude that the deep discharge at a potential below 3 V may cause a change in the crystal structure of the cathode and thus a change in the behavior of the ASI. This reduction in ASI values, and hence the increase of Li-ion diffusion, may be attributed to a partial spinel-like order, $Li_{1+y}Mn_{2-y}O_4$, and a partial phase transition $Li_2Mn_2O_4$ from ideal spinel $LiMn_2O_4$.

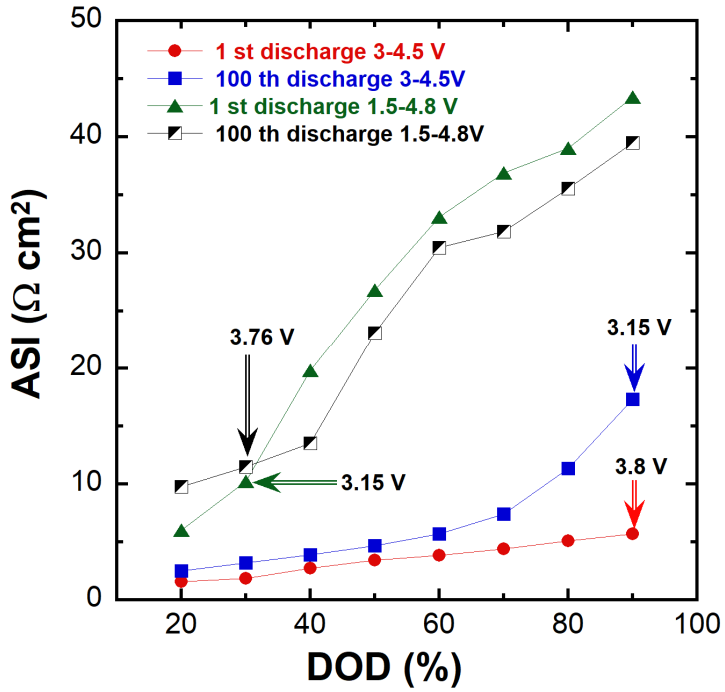


**Figure 12**. Area-specific impedance of the LMO900 electrode as a function of depth of discharge (DOD) for the 1st and the 100th cycle. Cells were operating in the narrow (3.0–4.5 V) and wide (1.5–4.8 V) potential window at 0.7 C rate.

### *3.7. Long-term Cycling Characterization*

To characterize the electrochemical performance of the cathode materials, differential capacity (d$Q$/d$V$ vs. $V$) plots are important indicators for tracking phase retention during cycling [34]. The curves d$Q$/d$V$ vs. $V$ presented in Figure 13 were calculated from GCD data reported in Figure 10b.

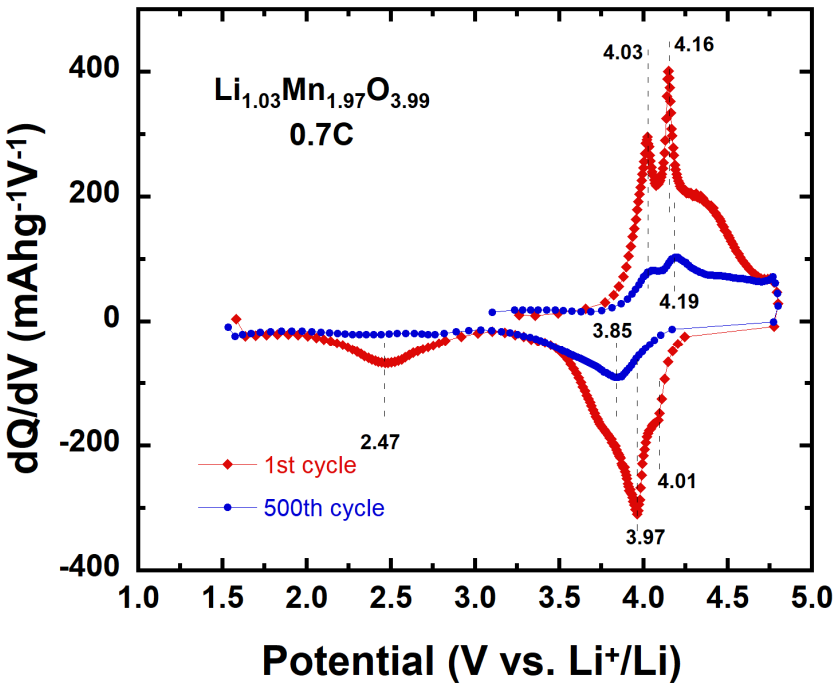


**Figure 13**. Differential capacity plots (d$Q$/d$V$) vs. $V$ for the LMO900 electrode tested at the 1st and 500th cycle in the potential window 1.5–4.8 V.

The peaks at ~4 and ~3 V in the d$Q$/d$V$ plots correspond to $Mn^{3.5+/4+}$ and $Mn^{3+/3.5+}$, respectively. In the high potential region, two pairs of redox peaks correspond to the two undistinguished plateaus of Figure 10b, indicating that lithium-ions were extracted and inserted into the spinel phase by a two-step process. The differential capacity plot at the charge stage had two sharp peaks at 4.03 and 4.16 V, and the discharge stage also showed two sharp peaks at 4.01 and 3.97 V.

The peak potential at 2.47 V corresponds to the pseudoplateau arising from the insertion of Li ions into the spinel 16*c* sites. Regarding the differential capacity after 500 cycles, all redox peaks maintain the same potential position; only their intensity decreases throughout cycling due to the capacity decay of the LMO electrode. The peak potential difference remains unchanged after 500 cycles, indicating the good electrochemical stability of this Li-rich electrode, in which doping mitigates the fading mechanisms. Therefore, the differential capacity analysis clearly shows that introducing excess Li in $LiMn_2O_4$ significantly decreases the rate of capacity degradation during charge-discharge cycling.

## 4. Discussion

Previous works have reported the beneficial effects of the substitution of $Mn^{3+}$ for Li by (i) increasing the average Mn oxidation state due to charge compensation, (ii) partly breaking the structural symmetry of the spinel structure, (iii) inhibiting irreversible phase transitions, (iv) improving the diffusion of $Li^+$ ions through the structure due to the Li-excess configuration that introduces two types of fast Li-ion migration channels [38], (v) acting as the pilar of the host structure [22]. A comparison of the structural properties of Li-rich LMO materials from the literature is provided in Table 4. XRD data indicate that cation mixing is more severe in Li-rich LMO than in $LiMn_2O_4$, which is also reflected by the $I_{(311)}/I_{(400)}$ ratios. In stoichiometric $LiMn_2O_4$, the relative intensity of the (311) peak is slightly higher than that of the (400) peak (e.g., $I_{(311)}/I_{(400)}$ = 1.005). When many Mn ions are replaced by Li ions, the intensity of the (311) peak significantly decreases. This is because the (311) crystal plane is primarily made up of Mn, and Li has a much lower atomic number (and scattering factor) compared to Mn.For $Li_{1.03}Mn_{1.97}O_{3.99}$, the $I_{(311)}/I_{(400)}$ ratio is 0.87, indicating the presence of an abundant amount of substitutions.

**Table 4**. Comparison of the structural properties of Li-rich LMO materials from the literature.

| Composition | Synthesis/Calcination Temperature (°C) | Cubic Parameter *a* (Å) | Ref. |
|---|---|---|---|
| $Li_{1.02}Mn_{1.98}O_{4.02}$ | Solid-state reaction ($MnCO_3$+LiOH)/800 | 8.235(1) | [17] |
| $Li_{1.03}Mn_{1.97}O_4$ | Solid-state reaction (LiOH+γ-$MnO_2$)/650 | 8.216(1) | [17] |
| $LiMn_2O_4$ | Solid-state reaction (MnOOH+LiOH)/900 | 8.248(1) | [18] |
| $Li_{1.05}Mn_{1.95}O_4$ | Solid-state reaction ($Li_2CO_3$+EMD-$MnO_2$)/800 | 8.225 | [19] |
| $Li_{1.06}Mn_{1.93}Al_{0.01}O_4$ | Sucrose-aided combustion ($Li_2CO_3$+$Mn^0$)/700 | 8.2151(4) | [21] |
| $Li_{1.05}Mn_{1.95}O_4$ | Solid-state reaction ($Li_2CO_3$+$MnO_2$)/750 | 8.2328 | [25] |
| $Li_{1.05}Mn_{1.95}O_4$ | Succinic acid-aided sol-gel (MnOAc+LiOH)/700 | 8.2212(6) | [29] |
| $Li_{1.04}Mn_{1.96}O_4$ | Solid-state reaction ($Li_2CO_3$+EMD-$MnO_2$)/750 | 8.2442 | [34] |
| $Li_{1.09}Mn_{1.91}O_4$ | Solid-state reaction ($Li_2CO_3$+EMD-$MnO_2$)/900 | 8.2318 | [34] |
| $Li_{1.10}Mn_{1.90}O_4$ | Solid-state reaction ($LiNO_3$+$Mn(NO_3)_2$)/800 | 8.223(1) | [35] |
| $Li_{1.04}Mn_{1.96}O_4$ | Citric acid-aided sol-gel (MnOAc+LiOH)/500 | 8.2131(9) | [39] |
| $Li_{1.05}Mn_{1.95}O_4$ | Solid-state reaction ($MnCO_3$+LiOH)/800 | 8.2307(4) | [40] |
| $Li_{1.02}Mn_{1.98}O_4$ | Solid-state reaction ($Li_2CO_3$+$MnO_2$)/700 | 8.2284(4) | [41] |
| $Li_{1.05}Mn_{1.95}O_4$ | Solid-state reaction ($LiNO_3$+$MnO_2$)/700 | 8.2216(7) | [41] |
| $Li_{1.05}Mn_{1.95}O_4$ | Solid-state reaction (β-$MnO_2$ rods+LiOH/800 | 8.235(2) | [42] |
| $Li_{1.09}Mn_{1.91}O_4$ | Spray pyrolysis (LiOH+$MnCO_3$)/800 | 8.224 | [43] |
| $Li_{1.03}Mn_{1.97}O_{3.99}$ | EDTA-assisted sol-gel (LiOAc+MnOAc)/900 | 8.2449(2) | this work |

The capacity fading in $LiMn_2O_4$ spinel has been attributed to Mn dissolution and surface reactions with the electrolyte, which consume the active cathode material and inhibit charge transport [71,72]. The extent of Mn dissolution depends on the disproportionation reaction of $Mn^{3+}$ in the spinel framework [19]. Among the factors affecting the electrochemical properties of $LiMn_2O_4$, the amount of $Mn^{3+}$ is crucial as it significantly influences the specific discharge capacity and capacity fading [73]. As the Jahn-Teller distortion is effectively suppressed by the partial substitution of $Li^+$ ions for $Mn^{3+}$ ions, there is reduced phase transformation, leading to improved stability of the spinel phase even after extended cycling (i.e., 500 cycles at 0.7 C rate in the wide potential range 1.5–4.8 V). Our findings underscore the significant role of Li doping in developing spinel cathodes with enhanced manganese activity for high-energy-density applications. Few literature reports [16,74,75] investigated the performance of $LiMn_2O_4$ at high current density (>0.1 C) amid a potential range of 2.0–4.8 V. Our work rigorously examined the performance of $LiMn_2O_4$ at a significantly higher current density of 100 mA $g^{-1}$ (approximately 0.7 C, seven times higher than reported in previous articles) and across a wider potential range (1.5–4.8 V). Table 5 compares our results with the literature, demonstrating that cycling at a wide voltage range significantly enhances initial capacity, capacity retention, and Coulombic efficiency. Notably, Siller and coworkers [76] suggested that nano-shaped particles and thin films have the potential to alleviate

the adverse effects of extending the potential window towards the 3-V plateau. The correlation between volumetric specific capacity and C-rate dependency is evident and appears to be strongly linked to particle size differences, impacting the lengths of diffusion paths. Consequently, the highest capacities are achieved when microparticles are cycled and packed within the 200–300 nm range, a size category that aligns with the dimensions of the as-prepared $Li_{1.03}Mn_{1.97}O_{3.99}$.

**Table 5**. Electrochemical performance of Li-rich spinel LMO cathodes. Cycle number is given in parenthesis.

| Material | Potential Range (V) | Specific Capacity (mAh $g^{-1}$) | Rate | Ref. |
|---|---|---|---|---|
| $LiMn_2O_4$ polycrystals | 2.0–4.8 | 115 | 50 mA $g^{-1}$ (50) | [16] |
| $Li_{1.25}Mn_{1.75}O_4$ | 1.5–4.8 | 200 | 50 mA $g^{-1}$ (50) | [23] |
| $Li_{1.004}Mn_{1.932}O_4$ | 3.5–4.5 | 100 | C/3 (1) | [24] |
| $Li_{1.09}Mn_{1.91}O_{3.992}$ | 3.0–4.3 | 104 | 0.2 C (50) | [31] |
| $Li_{1.09}Mn_{1.91}O_4$ | 3.3–4.3 | 105 | 0.1 C (100) | [32] |
| $Li_{1.04}Mn_{1.96}O_4$ | 3.0–4.3 | 80 | 40 mA $g^{-1}$ (100) | [38] |
| $Li_{1.02}Mn_{1.98}O_4$ | 3.6–4.3 | 100 | 0.1 mA $cm^{-2}$ (20) | [41] |
| $Li_{1.05}Mn_{1.95}O_4$ nanorods | 3.5–4.3 | 75 | 2 C (100) | [42] |
| $Li_{1.09}Mn_{1.91}O_4$ | 3.5–4.3 | 85 | 10 C (100) | [43] |
| $Li_{1.05}Mn_{1.95}O_4$ | 3.0–4.3 | 75 | 0.3 C (100) | [58] |
| $Li_{1.028}Mn_2O_4$ | 2.9–4.4 | 117 | 0.1 mA $cm^{-2}$ (1) | [74] |
| $Li_{1.15}K_{0.05}Mn_{1.79}O_4$ | 3.3–4.3 | 76 | C/10 (380) | [77] |
| $Li_{1.08}MnO_4$ | 3.0–4.2 | 109 | 0.2 C (16) | [78] |
| $Li_{1.03}Mn_{1.97}O_{3.99}$ | 3.0–4.5 | 46 | 100 mA $g^{-1}$ (100) | this work |
| $Li_{1.03}Mn_{1.97}O_{3.99}$ | 1.5–4.8 | 123 | 100 mA $g^{-1}$ (100) | this work |
| $Li_{1.03}Mn_{1.97}O_{3.99}$ | 1.5–4.8 | 77 | 100 mA $g^{-1}$ (500) | this work |

These findings prompt additional observations. Generally, an elevation in the charging current leads to heightened polarization, as evident in the GCD profiles. However, there is no notable difference in the polarization degree when expanding the voltage window compared to operating within the narrow range (Figure 10a). The diminished electrode resistance observed in $Li_{1.03}Mn_{1.97}O_{3.99}$ is ascribed to the enhanced stability of the $MnO_6$ octahedra within the spinel framework, facilitated by the robust ionic Mn−O bonds formed through Li doping. Electronic conduction in $LiMn_2O_4$ is primarily facilitated by the hopping of small polarons, constituting the dominant contribution to the overall conductivity. Concurrently, ionic conduction occurs through the migration of lithium vacancies and/or interstitial ions [27]. Another noteworthy phenomenon is the diminishing plateau associated with the tetragonal phase (indicated by an arrow in Figure 10b), which gradually disappears with increasing current density. This finding implies that the tetragonal phase behaves similarly to a cubic phase under high current density conditions. The relatively high capacity and excellent capacity retention of the Li-rich spinel $Li_{1.03}Mn_{1.97}O_{3.99}$ are attributed to cationic disordering, including excess Li at Mn sites and Li/Mn exchange. This disordering intrinsically suppresses the cooperative Jahn-Teller distortion (CJTD) of $Mn^{3+}O_6$ octahedra, providing access to capacities beyond a single lithium intercalation. Performing ab initio calculations, Zuo and coworkers [23] demonstrated that cationic disordering could break the symmetry of $Mn^{3+}$ arrangements, disrupting the correlation of distortions arising from individual Jahn-Teller centers. This disruption prevents the $Mn^{3+}$-O bonds from distorting in one direction. Consequently, the LMO material is activated and can host extra Li-ion storage sites to deliver double capacity with good reversible cycling stability.

## 5. Conclusions

In summary, for the first time, we successfully induced the formation of the tetragonal phase $Li_2Mn_2O_4$ through long-term electrochemical cycling (over 500 cycles) of the Li-rich spinel $Li_{1.03}Mn_{1.97}O_{3.99}$ in the extended voltage range of 1.5–4.8 V, taking advantage of this continuous and elusive phenomenon known as Jahn-Teller distortion. Cycling spinel $LiMn_2O_4$ in the wide voltage range of 1.5–4.8 V enhances the initial specific capacity and reduces capacity decay more effectively compared to the narrow voltage range of 3.0–4.5 V, even at a relatively high current density of 100 mA $g^{-1}$. The improvement in electrochemical performance may be attributed to the increased amount of $Li^+$ ions passing through tetrahedral sites or 16*c* octahedral sites with no face-sharing Mn ions, resulting in lower electrostatic repulsion compared to passing through tetrahedra that share faces with one Mn ion. The $Li_{1.03}Mn_{1.97}O_{3.99}$ spinel electrode spinel electrode demonstrates superior rate capability (specific capacity at a rate of 100 mA $g^{-1}$, ~0.7 C) at ambient temperature,

coupled with good stability. This is achieved without intentional coating or doping with foreign ions, resulting in improved Li transport kinetics and, consequently, enhanced electrochemical behavior.

## Author Contributions

Conceptualization, A.M.H.; formal analysis, S.M.A., M.G.F., R.S.E.-T., S.G.M.; investigation, S.M.A., M.G.F., R.S.E.-T., S.G.M.; data curation, S.M.A., M.G.F., R.S.E.-T., S.G.M., A.E.A.; experimentation, A.E.A.-G.; writing—original draft, A.E.A.-G., A.M.H.; writing—review & editing, A.M., C.M.J.

## Ethics Statement

Not applicable.

## Informed Consent Statement

Not applicable.

## Funding

The authors declare no financial support for the research, authorship, or publication of this article.

## Declaration of Competing Interest

The authors declare that they have no known competing financial interests or personal relationships that could have appeared to influence the work reported in this paper.

## References

1. Goodenough JB, Park KS. The Li-ion rechargeable battery: A perspective. *J. Am. Chem. Soc.* **2013**, *135*, 1167–1176.
2. Schmuch R, Wagner R, Hörpel G, Placke T, Winter M. Performance and cost of materials for lithium-based rechargeable automotive batteries. *Nat. Energy* **2018**, *3*, 267−278.
3. Global EV Outlook 2023, IEA, Paris. Available online: https://www.iea.org/reports/global-ev-outlook-2023/ (accessed 6 April 2023).
4. Julien CM, Mauger A, Zaghib K, Groult H. Comparative issues of cathode materials for Li-ion batteries. *Inorganics* **2014**, *2*, 132–154.
5. Thackeray MM, Johnson PJ, De Picciotto LA, Bruce PG, Goodenough JB. Electrochemical extraction of lithium from $LiMn_2O_4$. *Mater. Res. Bull.* **1984**, *19*, 179–187.
6. Lee S, Cho Y, Song HK, Lee KT, Cho J. Carbon-coated single-crystal $LiMn_2O_4$ nanoparticle clusters as cathode material for high-energy and high-power lithium-ion batteries. *Angew. Chem. Int. Ed.* **2012**, *51*, 8748–8752.
7. Thackeray MM, Amine K. $LiMn_2O_4$ spinel and substituted cathodes. *Nat. Energy* **2021**, *6*, 566.
8. Zhu C, Nobuta A, Saito G, Nakatsugawa I, Akiyama T. Solution combustion synthesis of $LiMn_2O_4$ fine powders for lithium ion batteries. *Adv. Powder Technol.* **2014**, *25*, 342–347.
9. Lee GJ, Abbas MA, Lee MD, Lee J, Lee J, Bang JH. Lithiation mechanism change driven by thermally induced grain fining and its impact on the performance of $LiMn_2O_4$ in lithium-ion batteries. *Small* **2020**, *16*, 2002292.
10. Liang J, Zhang R, Li H, Wang L, Cai Z, Yan H, et al. The electrochemical mechanism of preparing Mn from $LiMn_2O_4$ in waste batteries in molten salt. *Crystals* **2021**, *11*, 1066.
11. David WIF, Thackeray MM, De Picciotto LA, Goodenough JB. Structure refinement of the spinel-related phases $Li_2Mn_2O_4$ and $Li_{0.2}Mn_2O_4$. *J. Solid. State Chem.* **1987**, *67*, 316–323.
12. Chung KY, Ryu CW, Kim KB. Onset mechanism of Jahn-Teller distortion in 4 V $LiMn_2O_4$ and its suppression by $LiM_{0.05}Mn_{1.95}O_4$ (M= Co, Ni) coating. *J. Electrochem. Soc.* **2005**, *152*, A791–A795.
13. Zheng H, Sun Q, Liu G, Song X, Battaglia VS. Correlation between dissolution behavior and electrochemical cycling performance for $LiNi_{1/3}Co_{1/3}Mn_{1/3}O_2$-based cells. *J. Power Sources* **2012**, *207*, 134–140.
14. Xu G, Liu Z, Zhang C, Cui G, Chen L. Strategies for improving the cyclability and thermo-stability of $LiMn_2O_4$-based batteries at elevated temperatures. *J. Mater. Chem. A* **2015**, *3*, 4092-4123.
15. Liu W, Kowal K, Farrington G. Electrochemical characteristics of spinel phase $LiMn_2O_4$-based cathode materials prepared by the Pechini process: Influence of firing temperature and dopants. *J. Electrochem. Soc.* **1996**, *143*, 3590–3596.
16. Yu F, Wang Y, Guo C, Liu H, Bao W, Li J, et al. Spinel $LiMn_2O_4$ cathode materials in wide voltage window: Single-crystalline versus polycrystalline. *Crystals* **2022**, *12*, 317.

17. Gummow RJ, de Kock A, Thackeray MM. Improved capacity retention in rechargeable 4 V lithium/lithium manganese oxide (spinel) cells. *Solid State Ion.* **1994**, *69*, 59−67.
18. Masquelier C, Tabuchi M, Ado K, Kanno R, Kobayashi Y, Maki Y, et al. Chemical and magnetic characterization of spinel materials in the $LiMn_2O_4$–$Li_2Mn_4O_9$–$Li_4Mn_5O_{12}$ system. *J. Solid State Chem.* **1996**, *123*, 255−266.
19. Du Pasquier A, Blyr A, Courjal P, Larcher D, Amatucci G, Gérand B, Tarascon JM. Mechanism for limited 55 °C storage performance of $Li_{1.05}Mn_{1.95}O_4$ electrodes. *J. Electrochem. Soc.* **1999**, *146*, 428-436.
20. Saitoh M, Sano M, Fujita M, Sakata M, Takata M, Nishibori E. Studies of capacity losses in cycles and storages for a $Li_{1.1}Mn_{1.9}O_4$ positive electrode. *J. Electrochem. Soc.* **2004**, *151*, A17−A22.
21. Amarilla JM, Petrov K, Pico F, Avdeev G, Rojo JM, Rojas RM. Sucrose-aided combustion synthesis of nanosized $LiMn_{1.99-y}Li_yM_{0.01}O_4$ ($M = Al^{3+}$, $Ni^{2+}$, $Cr^{3+}$, $Co^{3+}$, y = 0.01 and 0.06) spinels. Characterization and electrochemical behavior at 25 and at 55 °C in rechargeable lithium cells. *J. Power Sources* **2009**, *191*, 591−600.
22. Xie Y, Jin Y, Xiang L. Tuning the nanoarea interfacial properties for the improved performance of Li-rich polycrystalline Li-Mn-O spinel. *ACS Appl. Mater. Interfaces* **2019**, *11*, 14796−14802.
23. Zuo C, Hu Z, Qi R, Liu J, Li Z, Lu J, et al. Double the capacity of manganese spinel for lithium-ion storage by suppression of cooperative Jahn-Teller distortion. *Adv. Energy Mater.* **2020**, *10*, 2000363.
24. Xia Y, Yoshio M. An investigation of lithium insertion into spinel structure Li-Mn-O compounds. *J. Electrochem. Soc.* **1996**, *142*, 825–833.
25. Stoyanova R, Gorova M, Zhecheva E. EPR of $Mn^{4+}$ in spinels $Li_{1+x}Mn_{2-x}O_4$ with $0 \le x \le 0.1$. *J. Phys. Chem. Solids* **2000**, *61*, 609–614.
26. Kopec M, Dygas JR, Krok F, Julien CM. XRD and FTIR structural studies of Li substituted $Li_{1+y}Mn_{2-y}O_4$ prepared by wet chemistry. *Electrochem. Soc. Symp. Proc.* **2005**, *14*, 69–77.
27. Dygas JR, Kopec M, Krok F, Julien CM. Relaxation of polaronic charge carriers in lithium manganese spinels. *J. Non-Cryst. Solids* **2007**, *353*, 4384–4389.
28. Sugiyama J, Mukai K, Ikedo Y, Russo PL, Suzuki T, Watanabe I, et al. Microscopic magnetic and structural nature of spinel $Li[Li_xMn_{2-x}]O_4$. *Phys. Rev. B* **2007**, *75*, 174424.
29. Kopec M, Dygas JR, Krok F, Mauger A, Gendron F, Julien CM. Magnetic characterization of $Li_{1+x}Mn_{2-x}O_4$ spinel ($0 \le x \le 1/3$). *J. Phys. Chem. Solids* **2008**, *69*, 955–966.
30. Kamazawa K, Nozaki H, Harada M, Mukai K, Ikedo Y, Iida K, et al. Interrelationship between $Li^+$ diffusion, charge, and magnetism in $^7LiMn_2O_4$ and $^7Li_{1.1}Mn_{1.9}O_4$ spinels: Elastic, inelastic, and quasielastic neutron scattering. *Phys. Rev. B.* **2011**, *83*, 094401.
31. Kim JM, Lee G, Kim BH, Hih YS, Lee GW, Kim HJ. Ultrasound-assisted synthesis of Li-rich mesoporous $LiMn_2O_4$ nanospheres for enhancing the electrochemical performance in Li-ion secondary batteries. *Ultrason. Sonochem.* **2012**, *19*, 627–631.
32. Liu T, Dai A, Lu J, Yuan Y, Xiao Y, Yu L, et al. Correlation between manganese dissolution and dynamic phase stability in spinel-based lithium-ion battery. *Nat. Commun.* **2019**, *10*, 4721.
33. Hoang K. Understanding the electronic and ionic conduction and lithium over-stoichiometry in $LiMn_2O_4$ spinel. *J. Mater. Chem. A.* **2014**, *2*, 18271–18280.
34. Gao Y, Reimers JN, Dahn JR. Changes in the voltage profile of $Li/Li_{1+x}Mn_{2-x}O_4$ cells as a function of x. *Phys. Rev. B.* **1996**, *54*, 3878–3883.
35. Martinez S, Sobrados I, Tonti D, Amarilla JM, Sanz J. Chemical vs. electrochemical extraction of lithium from the Li-excess $Li_{1.10}Mn_{1.90}O_4$ spinel followed by NMR and DRX techniques. *Phys. Chem. Chem. Phys.* **2014**, *16*, 3282–3291.
36. Rodriguez-Carjaval J. Recent developments of the program FULLPROF. *Commission on Powder Diffraction (IUCr). Newsletter* **2001**, *26*, 12–19.
37. Schroeder AB, Dobdon ETA, Rueden CT, Tomancak P, Jug F, Eliceiri KW. The ImageJ ecosystem: Open-source software for image visualization, processing and analysis. *Protein Sci.* **2021**, *30*, 234–249.
38. Xiao W, Xin C, Li S, Jie J, Gu Y, Zheng J, et al. Insight into fast Li diffusion in Li-excess spinel lithium manganese oxide. *J. Mater. Chem. A.* **2018**, *6*, 9893−9898.
39. Li Y, Lin Z, Li Y, Chen C, He Y, Yang X. Preparation and electrochemical properties of Li-rich spinel type lithium manganate coated $LiMn_2O_4$. *Mater. Res. Bull.* **2011**, *46*, 2450−2455.
40. Bianchini M, Suard E, Croguennec L, Masquelier C. Li-rich $Li_{1+x}Mn_{2-x}O_4$ spinel electrode materials: An *operando* neutron diffraction study during $Li^+$ extraction/insertion. *J. Phys. Chem. C.* **2014**, *118*, 25947–25955.
41. Komaba S, Kumagai N, Sasaki T, Miki Y. Manganese dissolution from lithium doped Li-Mn-O spinel cathode materials into electrolyte dissolution. *Electrochemistry* **2001**, *69*, 784–787.
42. Ahn D, Gim J, Shin N, Koo YM, Kim J, Shin TJ. Nanorod-assembled spinel $Li_{1.05}Mn_{1.95}O_4$ rods with a central tunnel along the rod-axis for high rate capability of rechargeable lithium-ion batteries. *Electrochim. Acta.* **2010**, *55*, 8888–8893.
43. Hirose S, Kodera T, Ogihara T. Synthesis and electrochemical properties of Li-rich spinel type $LiMn_2O_4$ powders by spray pyrolysis using aqueous solution of manganese carbonate. *J. Alloys Compd.* **2010**, *506*, 883–887.

44. Williamson GK, Hall WH. X-ray line broadening from filed aluminium and wolfram. *Acta Metall.* **1953**, *1*, 22–31.
45. Abbas SM, Hashem AM, Abdel-Ghany AE, Ismail EH, Kotlár M, Winter M, et al. Ag-modified $LiMn_2O_4$ cathode for lithium-ion batteries: Coating functionalization. *Energies* **2020**, *13*, 5194.
46. Arrebola JC, Cballero A, Hernan L, Morales J. Improving the performance of lithium-ion batteries by using spinel nanoparticles. *J. Nanomater.* **2008**, *2008*, 659397.
47. Massarotti V, Bini M, Capsoni D. Structural and defect study of $LiMn_2O_4$ formation. *Z. Naturforsch. A* **1996**, *51*, 267–276.
48. Chen Y, Xie K, Pan Y, Zheng C. Effect of calcination temperature on the electrochemical performance of nanocrystalline $LiMn_2O_4$ prepared by a modified resorcinol-formaldehyde route. *Solid State Ion.* **2010**, *181*, 1445–1450.
49. Hashem AM, Abbas SM, Hou X, Eid AE, Abdel-Ghany AE. Facile one step synthesis method of spinel $LiMn_2O_4$ cathode material for lithium batteries. *Heliyon* **2019**, *5*, e02027.
50. Lee Y, Sun YK, Nahm KS. Synthesis of spinel $LiMn_2O_4$ cathode material prepared by an adipic acid-assisted sol–gel method for lithium secondary batteries. *Solid State Ion.* **1998**, *109*, 285–294.
51. Sun YK. Synthesis and electrochemical studies of spinel $Li_{1.03}Mn_2O_4$ cathode materials prepared by a sol-gel method for lithium secondary batteries. *Solid State Ion.* **1997**, *100*, 115–125.
52. Kebede MA. An investigation of the lattice parameter and micro-strain behaviour of $LiMn_2O_4$ coated with $LiMn_{1.5}Ni_{0.5}O_4$ to attain high-rate capability and cycling stability. *J. Energy Storage* **2023**, *72*, 108602.
53. Kim J, Kim K, Cho W, Shin WH, Kanno R, Choi JW. A truncated manganese spinel cathode for excellent power and lifetime in lithium-ion batteries. *Nano Lett.* **2012**, *12*, 6358–6365.
54. Huang SS, Wu H, Chen PH, Guo Y, Nie B, Chen BJ, et al. Facile pH-mediated synthesis of morphology-tunable $MnCO_3$ and their transformation to truncated octahedral spinel $LiMn_2O_4$ cathode materials for superior lithium storage. *J. Mater. Chem. A* **2015**, *3*, 3633–3640.
55. Hwang BM, Kim SJ, Lee YW, Park HC, Kim DM, Park KW. Truncated octahedral $LiMn_2O_4$ cathode for high-performance lithium-ion batteries. *Mater. Chem. Phys.* **2015**, *158*, 138–143.
56. Jiang C, Tang Z, Wang S, Zhang Z. A truncated octahedral spinel $LiMn_2O_4$ as high-performance cathode material for ultrafast and long-life lithium-ion batteries. *J. Power Sources* **2017**, *357*, 144–148.
57. Sun W, Cao F, Liu Y, Zhao X, Liu X, Yuan J. Nanoporous $LiMn_2O_4$ nanosheets with exposed {111} facets as cathodes for highly reversible lithium-ion batteries. *J. Mater. Chem.* **2012**, *22*, 20952–20957.
58. Jiao F, Bao J, Hill AH, Bruce PG. Synthesis of ordered mesoporous Li-Mn-O spinel as a positive electrode for rechargeable lithium batteries. *Angew. Chem. Int. Ed.* **2008**, *120*, 9857–9862.
59. Ramana CV, Massot M, Julien CM. XPS and Raman spectroscopic characterization of $LiMn_2O_4$ spinels. *Surf. Interface Anal.* **2005**, *37*, 412–416.
60. Cotte S, Pecquenard B, Le Cras F, Grissa R, Martinez H, Bourgeois L. Lithium-rich manganese oxide spinel thin films as 3 V electrode for lithium batteries. *Electrochim. Acta.* **2015**, *180*, 528–534.
61. Beyreuther E, Thiele C, Dörr K. XPS investigation of Mn valence in lanthanum manganite thin films under variation of oxygen content. *Phys. Rev. B* **2006**, *73*, 155425.
62. Hashem AM, Abdel-Ghany AE, Abuzeid HM, El-Tawil RS, Indris S, Ehrenberg H, et al. EDTA as chelating agent for sol-gel synthesis of spinel $LiMn_2O_4$ cathode material for lithium batteries. *J. Alloys Compd.* **2018**, *737*, 758–766.
63. Xu C, Li J, Feng X, Zhao J, Tang C, Ji B, et al. The improved performance of spinel $LiMn_2O_4$ cathode with micro-nanostructured sphere-interconnected-tube morphology and surface orientation at extreme conditions for lithium-ion batteries. *Electrochim. Acta.* **2020**, *358*, 136901.
64. Huang W, Zhang M, Liu T, Zhao W, He L, Yin L, et al. Tunning the linkage of structure units to enable stable spinel-based cathode in the wide potential window. *Nano Energy* **2021**, *89*, 106457.
65. Abou-Rjeily J, Bezza I, Laziz NA, Autret-Lambert C, Sougrati MT, Ghamouss F. High-rate cyclability and stability of $LiMn_2O_4$ cathode materials for lithium-ion batteries from low-cost natural β-$MnO_2$. *Energy Storage Mater.* **2020**, *26*, 423–432.
66. Put B, Vereecken PM, Labyedh N, Sepulveda A, Huyghebaert C, Radu IP, et al. High cycling stability and extreme rate performance in nanoscaled $LiMn_2O_4$ thin films. *ACS Appl. Mater. Interfaces.* **2015**, *7*, 22413−22420.
67. Li A, Shao Z, Yang S, Li X, Zhang A. Precipitation synthesis and enhanced electrochemical performance of graphene-modified $LiMn_2O_4$ for lithium-ion batteries. *Ionics* **2020**, *26*, 3231−3238.
68. Bard AJ, Faulkner LR. Electrochemical Methods: Fundamentals and Applications; Wiley & Sons, Inc.: New York, NY, USA, 2001; pp. 226–260.
69. Kuwata N, Nakane M, Miyazaki T, Mitsuishi K, Kawamura J. Lithium diffusion coefficient in $LiMn_2O_4$ thin films measured by secondary ion mass spectrometry with ion-exchange method. *Solid State Ion.* **2018**, *320*, 266–271.
70. Amine K, Liu J, Kang S, Belharouak I, Hyung Y, Vissers D, et al. Improved lithium manganese oxide spinel/graphite Li-ion cells for high-power applications. *J. Power Sources* **2004**, *129*, 14–19.
71. Hirayama M, Ido H, Kim K, Cho W, Tamura K, Mizuki J, et al. Kanno R. Dynamic structural changes at $LiMn_2O_4$/electrolyte interface during lithium battery reaction. *J. Am. Chem. Soc.* **2010**, *132*, 15268–15276.

72. Simmen F, Foelske-Schmitz A, Verma P, Horisberger M, Lippert T, Novák P, et al. Surface layer formation on $Li_{1+x}Mn_2O_{4-\delta}$ thin film electrodes during electrochemical cycling. *Electrochim. Acta.* **2011**, *56*, 8539–8544.
73. Chung HT, Myung ST, Cho TH, Son JT. Lattice parameter as a measure of electrochemical properties of $LiMn_2O_4$. *J. Power Sources* **2001**, *97–98*, 454–457.
74. Haruna AB, Barrett DH, Rodella CB, Erasmus RM, Venter AM, Sentsho ZN, et al. Microwave irradiation suppresses the Jahn-Teller distortion in spinel $LiMn_2O_4$ cathode material for lithium-ion batteries. *Electrochim. Acta.* **2022**, *426*, 140786.
75. Sharifidarabad H, Zakeri A, Adeli M. Preparation of spinel $LiMn_2O_4$ cathode material from used zinc-carbon and lithium-ion batteries. *Ceram. Int.* **2022**, *48*, 6663–6671.
76. Siller V, Gonzalez-Rosillo JC, Eroles MN, Baiutti F, Liedke MO, Butterling M, et al. Nanoscaled $LiMn_2O_4$ for extended cycling stability in the 3 V plateau. *ACS Appl. Mater. Interfaces* **2022**, *14*, 33438–33446.
77. Falqueto JB, Clark AH, Glen AS, Smales GJ, Vaz CAF, Schuler AJ, et al. High performance doped Li-rich $Li_{1+x}Mn_{2-x}O_4$ cathodes nanoparticles synthesized by facile, fast, and efficient microwave-assisted hydrothermal route. *ACS Appl. Energy Mater.* **2022**, *5*, 8357–8370.
78. Chan HW, Duh JG, Sheen SR. $LiMn_2O_4$ cathode doped with excess lithium and synthesized by co-precipitation for Li-ion batteries. *J. Power Sources* **2003**, *115*, 110–118.